2014

Dynamic and Double-Diffusive Instabilities in a Weak Pycnocline. Part II: Direct Numerical Simulations and Flux Laws

Flanagan, Jason D.; Radko, Timour; Shaw, William J.; Stanton, Timothy P.

Flanagan, Jason D., et al. "Dynamic and double-diffusive instabilities in a weak pycnocline. Part ii: Direct numerical simulations and flux laws." Journal of Physical Oceanography44.8 (2014): 1992-2012.
http://hdl.handle.net/10945/62329

Dynamic and Double-Diffusive Instabilities in a Weak Pycnocline. Part II: Direct Numerical Simulations and Flux Laws

JASON D. FLANAGAN, TIMOUR RADKO, WILLIAM J. SHAW, AND TIMOTHY P. STANTON

Department of Oceanography, Naval Postgraduate School, Monterey, California

(Manuscript received 21 February 2013, in final form 13 May 2014)

ABSTRACT

This study examines the interaction of diffusive convection and shear through a series of 2D and 3D direct numerical simulations (DNS). The model employed is based on the Boussinesq equations of motion with oscillating shear represented by a forcing term in the momentum equation. This study calculates thermal diffusivities for a wide range of Froude numbers and density ratios and compares the results with those from the analysis of observational data gathered during a 2005 expedition to the eastern Weddell Sea. The patterns of layering and the strong dependence of thermal diffusivity on the density ratio described here are in agreement with observations. Additionally, the authors evaluate salinity fluxes that are inaccessible from field data and formulate a parameterization of buoyancy transport. The relative significance of double diffusion and shear is quantified through comparison of density fluxes, efficiency factor, and dissipation ratio for the regimes with/without diffusive convection. This study assesses the accuracy of the thermal production dissipation and turbulent kinetic energy balances, commonly used in microstructure-based observational studies, and quantifies the length of the averaging period required for reliable statistics and the spatial variability of heat flux.

1. Introduction

Much of the small-scale mixing that occurs within the stable ocean interior is believed to be the result of instabilities produced by either double diffusion or shear. Double diffusion can occur in a fluid whose density is determined by two components with differing molecular diffusivities, a condition naturally met in the World Ocean where the diffusivity of salt is two orders of magnitude less than that of heat. There are two modes of double diffusion possible, salt fingering and diffusive convection. For salt fingering to occur, both temperature T and salinity S decrease with depth, that is, $T_z,\ S_z > 0$. Such conditions are met in almost one-third of the World Ocean and are prevalent in the main thermocline (You 2002). Diffusive convection occurs in areas where both temperature and salinity increase with depth, that is, $T_z,\ S_z < 0$. Within the World Ocean, these conditions are typically met in high latitudes—regions that have traditionally been less accessible (due to seasonal ice cover, for instance) than those where salt fingering is active. Such regional inaccessibility has led to a bias toward the study of the salt fingering mode. For instance, much is known of the interaction of the salt fingering mode and shear (e.g., Kimura et al. 2011)—typically, shear reduces thermal and saline diffusivities (Kunze 1994). By contrast, the opposite effect has been suggested (Padman 1994) in the case of the diffusive convective mode in the presence of dynamically stable shear.

This study, which focuses on the diffusive mode, is the second in a series that has been motivated by observational data gathered during a 2005 expedition to the eastern Weddell Sea—a description of these data is presented in a companion study (Shaw and Stanton 2014, hereafter referred to as Part I). As part of the Maud Rise Nonlinear Equation of State Study (MaudNESS), the purpose of this expedition was to examine water column stability in the vicinity of Maud Rise, where large intermittent polynyas have been observed. These polynyas are indicative of deep convection, while their intermittent character is indicative of the weak but persistent nature of the water column in austral wintertime conditions that maintain a thin ice cover. Such polynyas can be explained by a "thermal barrier" negative feedback, whereby heat transported to the surface from a weakened pycnocline and warm deep water prohibits the formation of sea ice

Corresponding author address: J. D. Flanagan, Graduate School of Engineering and Applied Sciences, Department of Oceanography, Naval Postgraduate School, Monterey, CA 93943.
E-mail: jdflanag@nps.edu

DOI: 10.1175/JPO-D-13-043.1

(Martinson 1990). The strength of this negative feedback is in part dependent on pycnocline turbulence, which is in turn forced by several possible processes, including diffusive convection and internal wave shear.

During the MaudNESS experiment, more than 1300 CTD/microstructure profiles of temperature and conductivity over the depth range 17–350 m were gathered, with salinity and density estimated at 10-cm intervals after processing, while estimates of shear were made from the shipboard acoustic Doppler current profiler (ADCP). Such refined temperature and conductivity data allow for the resolution of diffusive convective layers that typically have vertical scales on the order of meters. The generation of well-mixed layers and their subsequent evolution through either merging and/or disintegration was detected. As described in Part I, subsequent analysis of observed thermal diffusivity k_T showed that k_T variability is dependent both on turbulence generated by shear and double diffusion. The intensity of shear is controlled by the Froude number

$$\mathrm{Fr} = |\mathbf{u}_z|/N = \mathrm{Ri}^{-1/2} \tag{1}$$

(where N is the buoyancy frequency and $|\mathbf{u}_z|$ is the shear magnitude), whereas double diffusion is controlled by the density ratio

$$R_\rho = \beta S_z/\alpha T_z, \tag{2}$$

where α, β are the coefficients of thermal expansion and haline contraction, respectively. For ensembles with relatively weak shear ($\mathrm{Fr} < 0.35$), k_T showed clear dependence on R_ρ and no clear dependence on Fr. Those with $R_\rho < 1.5$ had higher diffusivities (by as much as an order of magnitude) than those with $R_\rho > 1.5$. For ensembles where $\mathrm{Fr} > 0.35$, the difference in diffusivities lessens—diffusivity values for large R_ρ approach those for small R_ρ.

Until recently, much of our understanding of double-diffusive vertical transport of heat came from laboratory experiments. Turner (1965) produced estimates based on the so-called four-thirds flux laws and, since then, numerous laboratory studies (Marmorino and Caldwell 1976; Newell 1984; Taylor 1988; Kelley 1990; among others) have focused on the calibration and/or validation of these laws. Lately, more attention has been paid to direct numerical simulations (DNS). For instance, the 3D DNS of Carpenter et al. (2012) and Flanagan et al. (2013) have shown that extant laboratory-derived flux laws (e.g., Marmorino and Caldwell 1976; Kelley 1990) can underestimate heat transport by as much as a factor of 2–3. Flanagan et al. (2013) attribute this discrepancy to the presence of rigid boundaries and the run-down character of experiments. See Radko (2013) for a recent review of laboratory, numerical, and observational results on diffusive convection.

This study makes a step toward realism by incorporating the effects of large-scale external shear and associated dynamic instabilities. We utilize 2D and 3D DNS to both interpret and expand upon the findings presented in Part I by exploring a wider range of the Froude number/density ratio parameter space than was present in the observations. The shearing force introduced to our model is sinusoidal in space and periodic in nature, with the proviso that $\mathrm{Ri} < 0.25$ for some fraction of its period. We show that a simplified model incorporating fixed-amplitude forcing and double diffusion adequately describes the dynamics and mixing characteristics observed in the Weddell Sea. We examine the differences between diagnostics based on "local" (~40 cm) and "outer" (~5 m) vertical scales and validate the parameterization of k_T described in Part I through a more complete investigation of the relevant (Fr, R_ρ) parameter space. Additionally, we estimate the vertical transport of salt, which is currently unachievable through observations alone. Furthermore, we examine the balance of thermal variance and quantify the averaging period required for validity of the associated Osborn and Cox (1972) method. We also identify the source of error in the Osborn–Cox relation and quantify its magnitude. We examine the balance of turbulent kinetic energy (TKE) suggested by Osborn (1980). For both thermal variance dissipation and TKE-based methods, we quantify the error of the isotropic assumption used in microstructure analysis, when applied to the double-diffusive regime. Finally, we quantify fundamentally double-diffusive effects through the analysis of two sets of 3D DNS—one with diffusive convection and one without. Density flux magnitudes in the double-diffusive case are substantially lower, which is consistent with the tendency of double diffusion to transport density in the upgradient sense.

This study is organized as follows: In section 2, we describe the model setup and present typical 2D and 3D DNS illustrating the dynamics of the regime where both shear and diffusive convection interact. In section 3, we present an analysis from a series of DNS with varying shear amplitude and density ratio. The differences between statistics generated from local and outer scales are illustrated. In section 4, we present our main findings—a parameterization of k_T and k_S based on outer-scale statistics. Numerical estimates of k_T are compared with those observed during the MaudNESS 2005 expedition and found to be in general agreement. In section 5, we test the applicability of the thermal production dissipation and TKE balances (isotropic and anisotropic) in both

the double-diffusive and non-double-diffusive regimes. Last, in section 6, we summarize and discuss the key findings.

2. Model description and preliminary experiments

Following Stern et al. (2001), we first separate $T(x, y, z, t)$ and $S(x, y, z, t)$ into the linear basic state $[\overline{T}(z), \overline{S}(z)]$ and the perturbation $[T'(x, y, z, t), S'(x, y, z, t)]$. The relevant equations are then the Boussinesq equations of motion coupled with a linear equation of state. The equations are expressed in terms of T' and S' and nondimensionalized according to $l = (\kappa_T \nu / g\alpha \overline{\overline{T}}_z)^{1/4}$ (length), l^2/κ_T (time), κ_T/l (velocity), and $\rho_0 \nu \kappa_T / l^2$ (pressure), where κ_T is the molecular diffusivity of heat, ν is the kinematic viscosity, g is the acceleration due to gravity, and ρ_0 is the reference density used in the Boussinesq approximation. This particular system of nondimensionalization has been successfully utilized in many recent double-diffusive studies (e.g., Radko 2003; Stellmach et al. 2011; Flanagan et al. 2013) and is discussed in greater detail in Radko (2013, chapter 1). In this study, $\overline{\overline{T}}_z = (T_{\text{top}} - T_{\text{bottom}})/H$ is the nominal background temperature gradient (calculated over the domain height H) that is constant in space and time. It should not be confused with the horizontally averaged temperature gradient $\overline{T}_z(z, t)$ that can evolve in time, resulting in step formation. In the Weddell Sea, typical values are $\kappa_T \sim 1.4 \times 10^{-7}\,\text{m}^2\,\text{s}^{-1}$, $\nu \sim 1.8 \times 10^{-6}\,\text{m}^2\,\text{s}^{-1}$, $\alpha \sim 6.5 \times 10^{-5}\,^\circ\text{C}^{-1}$, and $\overline{\overline{T}}_z \sim 5 \times 10^{-2}\,^\circ\text{C}\,\text{m}^{-1}$. Therefore, in what follows, $l \sim 1 \times 10^{-2}\,\text{m}$. Finally, αT and βS are both scaled by $\alpha \overline{\overline{T}}_z l$, leading to the set of nondimensional equations:

$$\frac{1}{\text{Pr}}\left(\frac{\partial \mathbf{u}}{\partial t} + \mathbf{u}\cdot\nabla\mathbf{u}\right) = -\nabla p + (T' - S')\hat{\mathbf{k}} + \nabla^2\mathbf{u} + \mathbf{f}_\mathbf{u}, \tag{3}$$

$$\nabla\cdot\mathbf{u} = 0, \tag{4}$$

$$\frac{\partial T'}{\partial t} + \mathbf{u}\cdot\nabla T' - \hat{\mathbf{k}}\cdot\mathbf{u} = \nabla^2 T', \quad \text{and} \tag{5}$$

$$\frac{\partial S'}{\partial t} + \mathbf{u}\cdot\nabla S' - R_\rho \hat{k}\cdot\mathbf{u} = \tau\nabla^2 S', \tag{6}$$

where $\mathbf{u}$ denotes the velocity field, $\hat{\mathbf{k}}$ is the vertical unit vector, and $f_\mathbf{u}$ represents external forcing of the velocity aimed to represent tidally driven motions. The quantities $\text{Pr} = \nu/\kappa_T$, $\tau = \kappa_S/\kappa_T$, and $R_\rho = \beta\overline{\overline{S}}_z/\alpha\overline{\overline{T}}_z$ are the Prandtl number, the molecular diffusivity ratio (Lewis number), and the density ratio, respectively. It is these three nondimensional numbers that govern how the above system evolves. Additionally, system (3)–(6) is solved in either a two- or three-dimensional periodic domain, with $\overline{\overline{T}}_z$ and $\overline{\overline{S}}_z$ maintained at constant values. Such a setup is designed to represent conditions found in the stable ocean interior, where boundaries and their effects are largely irrelevant.

Since this study is focused on the interaction of shear with double-diffusive processes in the Weddell Sea region, where the water column is susceptible to turbulent instabilities generated by internal waves, we choose a temporally oscillating sinusoidal shearing force such that

$$f_\mathbf{u} = \hat{\mathbf{i}} A \sin(mz)\cos(\omega t), \tag{7}$$

where $\hat{\mathbf{i}}$ is the unit vector in the x direction, $m = 2\pi/H$ is the vertical wavenumber, $\omega = 2\pi f$ is the angular frequency, and A and f describe the shearing force amplitude and frequency, respectively. We choose the period $f^{-1} = 20\pi$ that, in dimensional units, gives a periodicity of $20\pi l^2/3600\kappa_T \sim 12$ hours. In the Weddell Sea, motions that generate shear typically display periods in the range 6–12 h (see Part I). The choice of A is determined by consideration of the well-known criterion that, for shear instability to arise, the Richardson number Ri must be less than ¼. In dimensional form (denoted by the asterisk superscript), this restriction is given by

$$\text{Ri} = \frac{\dfrac{g}{\rho_0^*}\dfrac{d\rho^*}{dz^*}}{\left(\dfrac{\partial \mathbf{u}^*}{\partial z^*}\right)^2} < \frac{1}{4}. \tag{8}$$

Upon nondimensionalization, the condition for shear instability (8) reduces to

$$4\text{Pr}(R_\rho - 1) < \left(\frac{\partial \mathbf{u}}{\partial z}\right)^2. \tag{9}$$

Finally, if $\mathbf{u}$ takes the form of an oscillating harmonic in both t and z [as in (7)], then (9) is reduced to the simple condition that A be greater than some critical value A_{cr}, where

$$A_{\text{cr}} = \frac{\omega}{m}\sqrt{4\text{Pr}(R_\rho - 1)}. \tag{10}$$

An initial 2D DNS on a nondimensional domain of size 1000×500 ($\sim 10\,\text{m} \times 5\,\text{m}$) was performed to examine the regime where critical shear has been introduced and double-diffusive processes are active. This DNS was conducted using a Message Passing Interface (MPI) pseudospectral code (Stern et al. 2001) developed specifically to solve the system of (3)–(6) and modified to allow for the introduction of the shearing force described by (7). In the ocean, the molecular diffusivity ratio τ typically has values on the order of

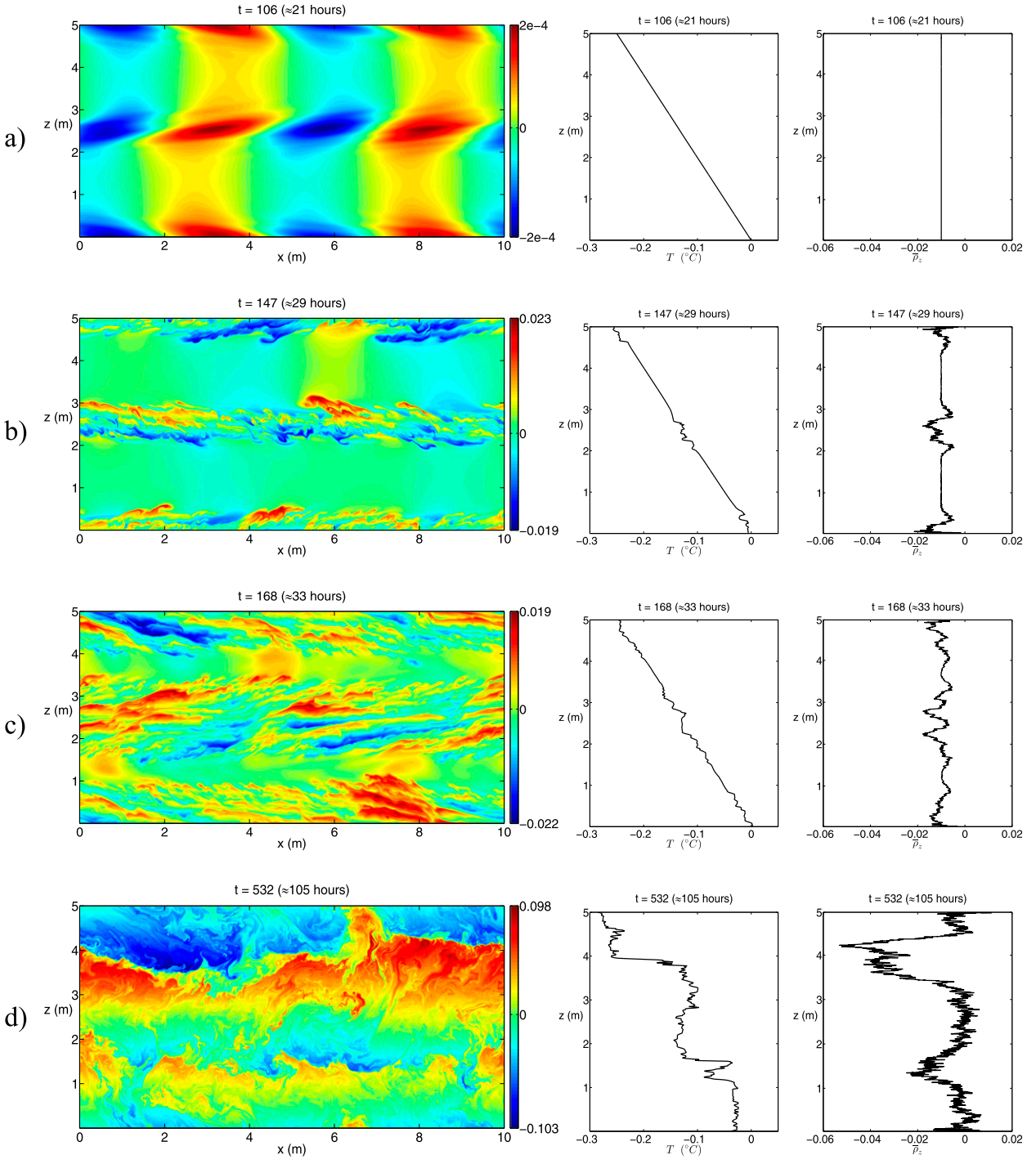

FIG. 1. (left) A time series of the temperature perturbation field T' taken from a 2D DNS with $\tau = 0.01$. (middle) Corresponding profiles of total temperature T at $x = 5$ m. (right) Corresponding profiles of the vertical gradient of horizontally averaged density $\overline{\rho}_z(z, t)$. (a) The initial instability takes the form of patches aligned along the lines $z = 0$, $H/2$, H at $t \approx 21$ h, after which (b),(c) layers are formed and subsequently merge to form (d) two distinct and persistent layers.

10^{-2}. Therefore, for this initial DNS, we set $\tau = 0.01$. For any DNS to be deemed realistic, it must resolve the scalar field with the smallest diffusivity—that is, the S' field—which in turn leads to a computationally expensive DNS. To satisfy this requirement we chose a grid of size 6144×3072. Both T' and S' were initialized by small-amplitude computer-generated random fields and the initial velocity field was zero: $\mathbf{u}(\mathbf{x}, t = 0) = 0$. To replicate conditions found in the Weddell Sea, we set $\mathrm{Pr} = 13$ and, for this initial experiment, $R_\rho = 1.2$. Substitution of these parameter values into (10) gives $A_{\mathrm{cr}} \cong 25.66$. To satisfy the Richardson condition, we let $A = 30$, which translates to supercritical shear ($\mathrm{Ri} < 1/4$) for ~36% of the shear forcing period.

The evolution over time of T' from this DNS is illustrated in Fig. 1. Also shown are the corresponding profiles of T (at $x = 5$ m, the center of the domain) and the vertical gradient of horizontally averaged density $\overline{\rho}_z(z, t)$. The initial perturbation grows to form distinct patches aligned along the lines of shearing force maximum at $z = 0, H/2, H$ by $t = 106$ (Fig. 1a), which, in dimensional units, equates to ~21 h. At $t = 147$ (≈29 h), layerlike formations and Kelvin-Helmholtz (K–H) instabilities (where $\mathrm{Ri} < 1/4$) are seen (Fig. 1b). Layers continue to develop (Fig. 1c) throughout the domain with subsequent layer merging observed for the remainder of the experiment. A representative example of a persistent layered structure from late in this simulation is shown in Fig. 1d, with $t = 532$ (≈106 h). Evidence of layer merging is visible in Fig. 2 where a time series of T profiles ($x = 5$ m) are shown. At $t = 260$, there are at least nine distinct layers. By $t = 267$, layer merging has reduced the number of layers to six. Mergers continue until there are only two layers remaining (at $t = 280$), with thicknesses that are likely determined by the (sinusoidal) shearing force (7).

Low values for τ require such fine resolution that a parameter sweep, even in a 2D DNS, becomes unfeasible. However, some properties are not particularly sensitive to the specific value of τ, provided that τ is considerably less than unity—a feature illustrated, albeit for salt fingers, by Stern et al. (2001). We have tested this conclusion for the diffusive convection in shear problem by examining the case where $\tau = 0.1$ in 2D. In Fig. 3, we present a time series of T' fields and T profiles from this DNS. Qualitatively, the dynamics are similar, with K–H instability, layer formation, merging and persistence apparent. Quantitatively, we have calculated (nondimensional) temperature, salinity, and buoyancy fluxes according to $F_{T'}(t) = \overline{w'T'}$, $F_{S'}(t) = \overline{w'S'}$, and $F_{\rho'}(t) = \overline{w'\rho'}$. For the case where $\tau = 0.01$, $\langle F_{T'} \rangle \approx 353.4$, $\langle F_{S'} \rangle \approx 344.9$, and $\langle F_{\rho'} \rangle \approx -8.5$, where the angled brackets denote time averaging after equilibration over the interval of statistically steady evolution, typically $\sim 3f^{-1} - 5f^{-1}$. For the $\tau = 0.1$ case, $\langle F_{T'} \rangle \approx 327.1$, $\langle F_{S'} \rangle \approx 347.5$, and $\langle F_{\rho'} \rangle \approx 20.4$ There are two important points to note. First, an increase in τ by an order of magnitude results in 7% and 1% changes in $\langle F_{T'} \rangle$ and $\langle F_{S'} \rangle$, respectively—giving confidence that DNS performed at higher τ are sufficiently accurate when evaluating individual property fluxes. Second, both the magnitude and sign of $\langle F_{\rho'} \rangle$ are different, which should be kept in mind when assessing the importance of double-diffusive effects.

The sensitivity of density fluxes to τ is also supported by the DNS, where $\tau = 1$ (Figs. 4 and 5),

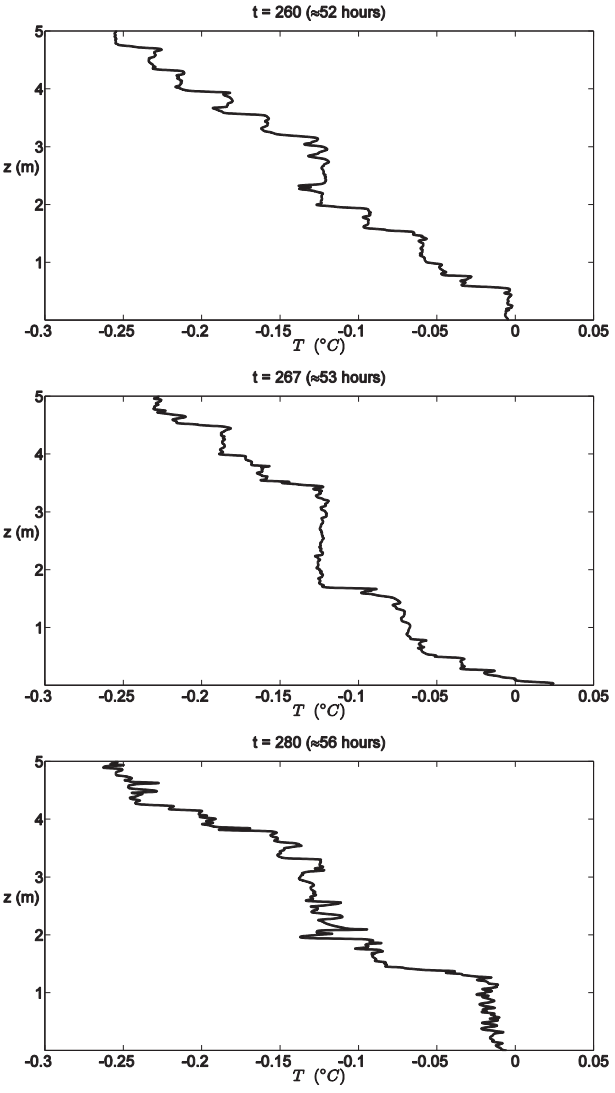

FIG. 2. An example of layer merging taken from the 2D DNS described in Fig. 1. Shown are typical profiles of total temperature T taken at the center of the 2D domain—that is, $x = 5$ m. (top) At $t \approx 52$ h, up to 10 distinct layers are visible. (middle) At $t \approx 53$ h, the number of layers has reduced to six. Layers continue to merge until (bottom) only two remain at $t \approx 56$ h.

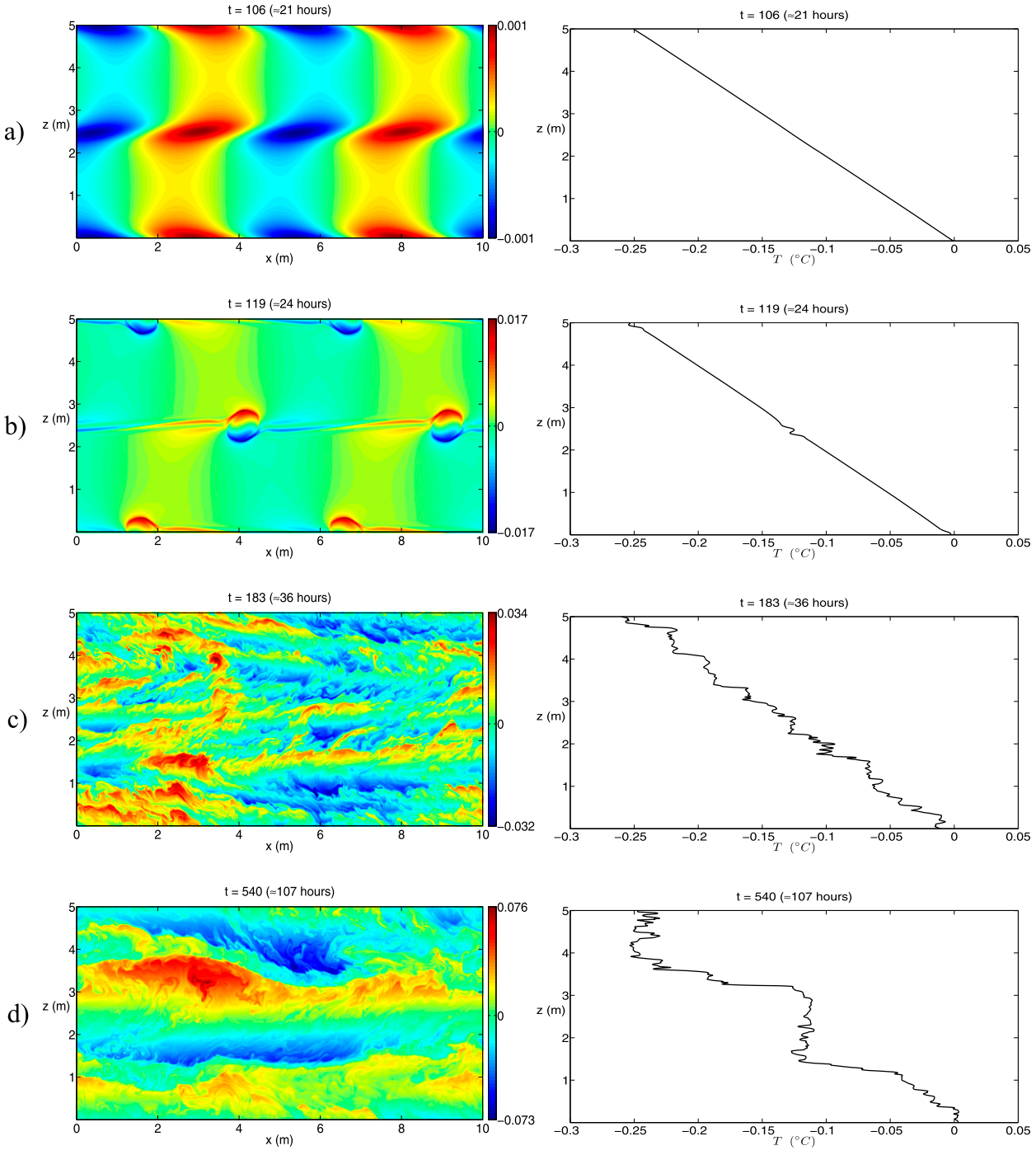

FIG. 3. From a 2D DNS identical to that in Fig. 1 but for $\tau = 0.1$. Shown are time series of (left) T' and (right) the corresponding profiles of total temperature T at $x = 5$ m. Represented are (a) the evolution of patches (≈21 h), (b) the onset of K–H instability (≈24 h), (c) initial layer formation (≈36 h), and (d) the persistence of layers (≈107 h).

representative of the case where double diffusion has effectively been "switched off." Again, the dynamics in this regime are qualitatively similar to those described for $\tau = 0.1, 0.01$ with the exception that no persistent layers were observed (Figs. 4d and 5). Here, $\langle F_{T'} \rangle \approx 319.9$, $\langle F_{S'} \rangle \approx 383.9$, and $\langle F_{\rho'} \rangle \approx 63.9$, further emphasizing the trend of relatively small change in $\langle F_{T'} \rangle$ and $\langle F_{S'} \rangle$, but large increase in $\langle F_{\rho'} \rangle$ as we move away from the double-diffusive regime.

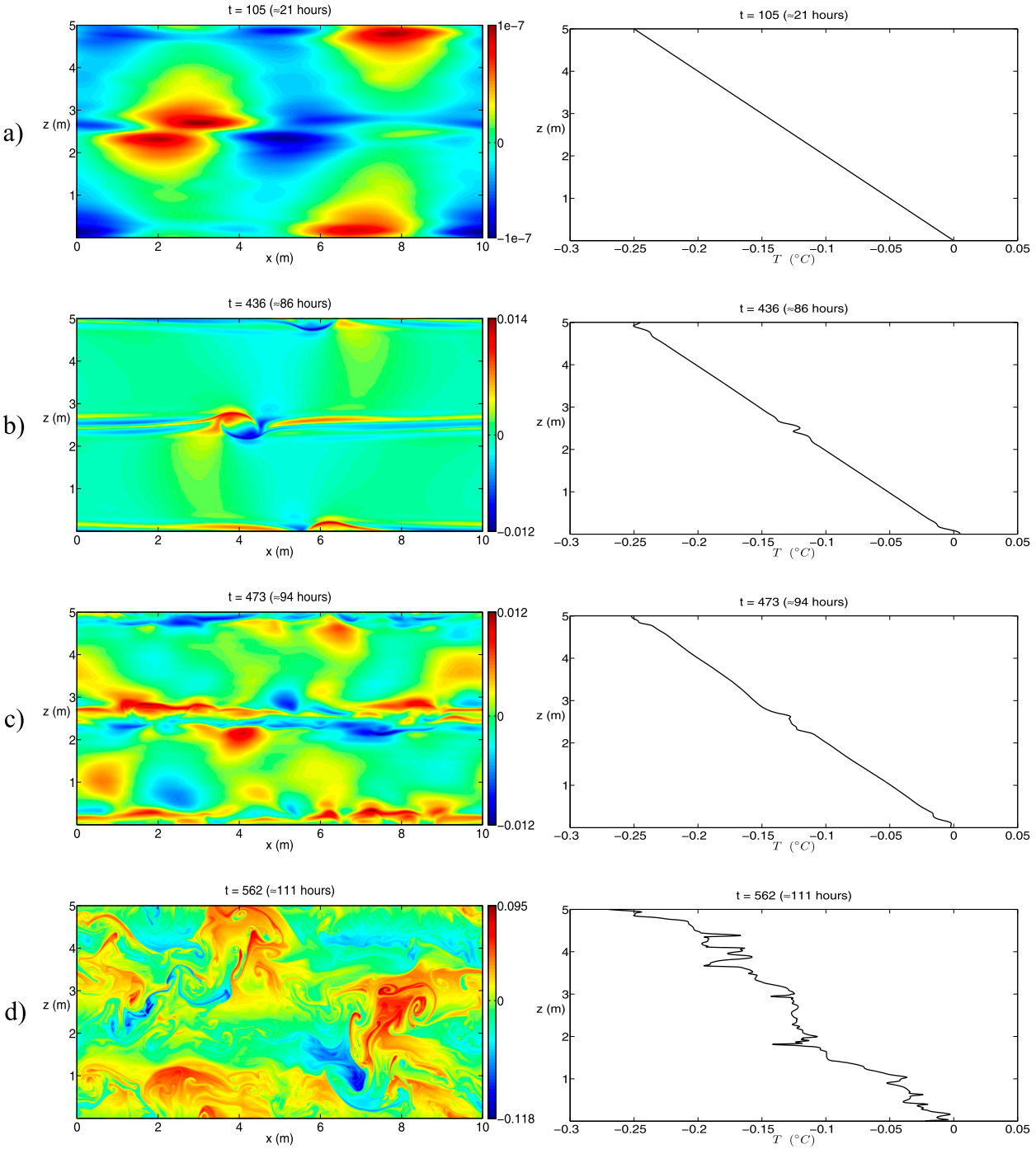

FIG. 4. From a 2D DNS identical to that in Fig. 3, but where double diffusion has been switched off by setting $\tau = 1$. Shown are time series of (left) T' and (right) the corresponding profiles of total temperature T at $x = 5$ m. Again (a) the evolution of patches (≈24 h) and (b) K–H instability (≈24 h) are readily observed. However, layer formations are no longer observed—(c),(d) comparison with Figs. 3c and 3d counterparts.

3. Modeled and observed diffusivities

In Part I, the dependence of thermal diffusivity k_T on Fr and R_ρ were examined with the conclusion that k_T is strongly dependent on R_ρ. To test this conclusion, we have conducted five 3D DNS and eight 2D DNS. The 2D DNS, by their very nature, are much less computationally expensive than 3D DNS, and one might be tempted to focus excessively on them, with potentially serious consequences. For instance, it is known that in 2D

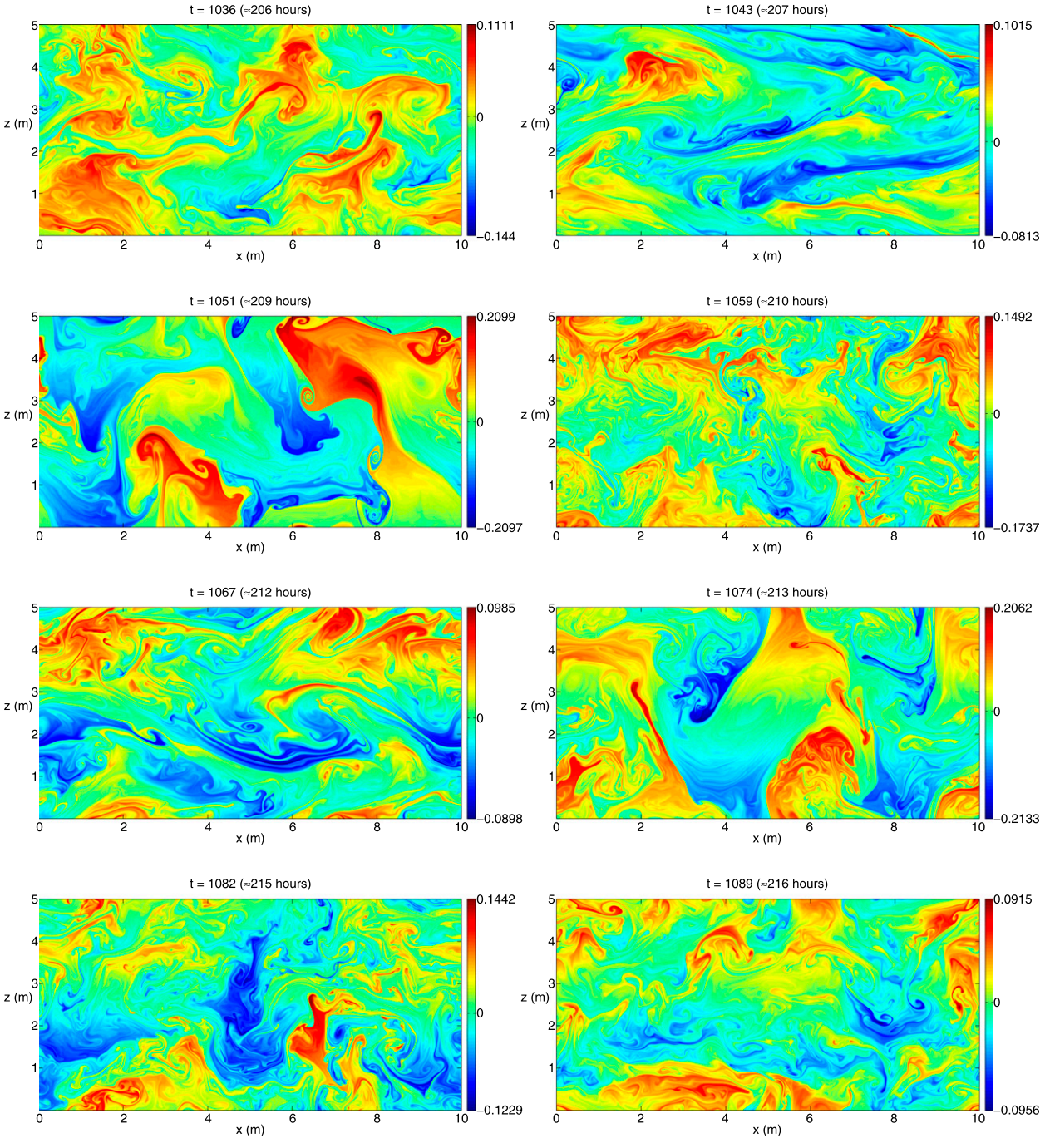

FIG. 5. Shown (from top left) is a time series of T' taken from the 2D DNS described in Fig. 4. The time range was chosen so as to cover the last recorded full period of shear forcing. As described in Fig. 4, and contrary to Fig. 3, no layering was evidenced throughout the duration of this DNS.

turbulence, there is an inverse energy cascade so that much of the TKE accumulates at large scales (Batchelor 1953). In 3D turbulence, vortex stretching provides the mechanism whereby energy cascades down to the smallest scales. Therefore, in what follows, we rely on 2D DNS only in a qualitative sense and derive all quantitative conclusions from our 3D DNS. Additionally, in consideration of computational efficiency, we examine the cases with $\tau = 1/3$ (3D) and $\tau = 0.1$ (2D). The significant double-diffusive effects observed in the following analysis suggest that double diffusion plays an even more profound role in the ocean where $\tau = 0.01$.

However, even such large values of τ require $1536 \times 384 \times 768$ (10 m $\times$ 2.5 m $\times$ 5 m) and 3072×1536 (10 m $\times$ 5 m) grid points, respectively, for the adequate resolution of S'. Each of T', S', and $\mathbf{u}$ were initialized as described in section 2 and again we set Pr = 13. In 3D, we have conducted five DNS with $R_\rho = 1.2$, 1.35, 1.5, 1.65 and 1.8, while in 2D we have conducted eight DNS with $R_\rho = 1.1, 1.2, \ldots, 1.8$. In all these experiments, we examined the case of fixed forcing amplitude by setting $A = 50$, thereby ensuring that the system was in the unstable regime (i.e., $A > A_{cr}$ and therefore, by extension, Ri $< 1/4$) for some fraction of the forcing period. From (10), $26 \lesssim A_{cr} \lesssim 51$ for the chosen range of (3D DNS) R_ρ. Therefore, $A > A_{cr}$ for ~65% of the shear forcing period when $R_\rho = 1.2$, with this percentage decreasing monotonically to zero when $R_\rho = 1.8$. Incidentally, interesting counterexamples to the Richardson criterion (see the appendix) in double-diffusive DNS have been observed.

In addition to experiments in which A was held constant, we performed the simulation where A continuously increased from 25 to 125. Fluxes diagnosed from this experiment matched those in fixed-amplitude forcing runs for corresponding values of A (Fig. 6). This consistency suggests that the equilibrium transport characteristics are fully determined by the present parameters and are independent of the past history of the system.

In all cases, we have found the 3D system to be qualitatively similar to 2D. For example, Fig. 7 illustrates the evolution over time of T' from the 3D DNS with $R_\rho = 1.5$. Also shown is the T profile obtained at the center of the domain (i.e., $x = 5$ m and $y = 1.25$ m). The initial perturbation (Fig. 7a) grows to form several layers by $t = 341$ (Fig. 7b), corresponding to 68 h. By $t = 388$ (77 h), these layers have merged (Fig. 7c) to form two layers spanning the entire domain and separated by interfaces aligned along the lines of minimum forcing, that is, $z = H/4$, $3H/4$, where $H = 500$ is the (nondimensional) height of the domain. These layers persist for the remainder of the experiment as seen in Fig. 7d where $t = 783$ (155 h). The persistent nature of these layers is further evidenced in Fig. 8 where we plot both T' and T, from the experiment shown in Fig. 7, at various times throughout a turbulent event. Here, $T = T' + \overline{\overline{T}}$ where the double overbar represents the background state. Well-mixed layers are seen at $t = 405$ (80 h) in Fig. 8a. These layers are disrupted at $t = 420$ (83 h) when the shearing force is close to maximum (Fig. 8b) and quickly reform when the forcing subsides, that is, at $t = 439$ (87 h) in Fig. 8c. This pattern of layer formation has been found to occur in all DNS conducted.

One of the key questions addressed by the observational component of this study (Part I) was the magnitude

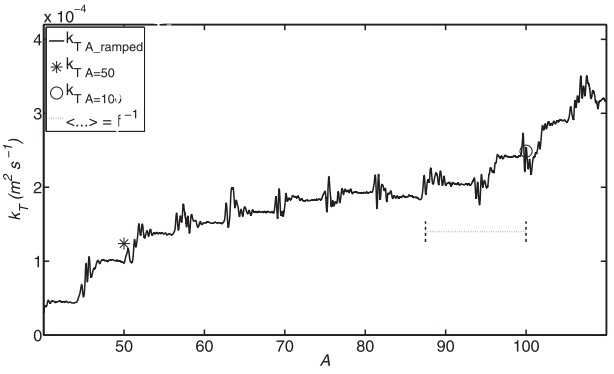

FIG. 6. A record of k_T from a 2D DNS where A is gradually increased (solid line). Estimate of $\langle k_T \rangle$ from a 2D DNS where (constant) $A = 50$ (asterisk). Estimate of $\langle k_T \rangle$ from a 2D DNS where (constant) $A = 100$ (circle). The time interval f^{-1} over which boxcar averaging was performed (dashed line).

and dependencies of vertical diffusivities, with diagnostics based on the Osborn–Cox production–dissipation balance. The estimates based on the Osborn–Cox balance depend on the chosen operational definition of finescale gradients. DNS affords the opportunity to examine the merits of balances based on a small, local vertical sale and the outer vertical scale defined by the model vertical boundary. Similar questions arise with respect to temporal variability. We are dealing with a nonlinear system and therefore systematic differences between local and outer-scale parameterizations could be expected. We have tackled the parameterization of k_T utilizing two techniques that differ according to the vertical scale over which the relevant quantities—Fr, R_ρ, and k_T—are calculated. The scales considered are at both the 0.4- (local) and 5-m (box height) levels and in what follows are denoted by the subscripts loc and b, respectively. The local scale (0.4 m) was chosen as a compromise between the desire to parameterize k_T at length scales greater than that over which double diffusion diffuses heat (~10 cm) and the need for a clear scale separation between local (inner) and box (outer) scales. For each method used, we considered data output only after the system had evolved into a fully turbulent state and $F_{T'}$ and $F_{S'}$ had fully equilibrated. To help determine whether equilibration had occurred, centered boxcar smoothing with box width f^{-1} has been employed. In Fig. 9, we present a typical case from the 2D DNS with $R_\rho = 1.2$.

For each DNS, the domain was first partitioned into vertical bins of size 0.4 m. Then, local quantities were calculated at this resolution according to

$$k_{T\_\mathrm{loc}} = \kappa_T \frac{\overline{|\nabla_{\mathrm{ms}} T'|^2}}{(\overline{T}_{z\_\mathrm{loc}})^2}, \tag{11}$$

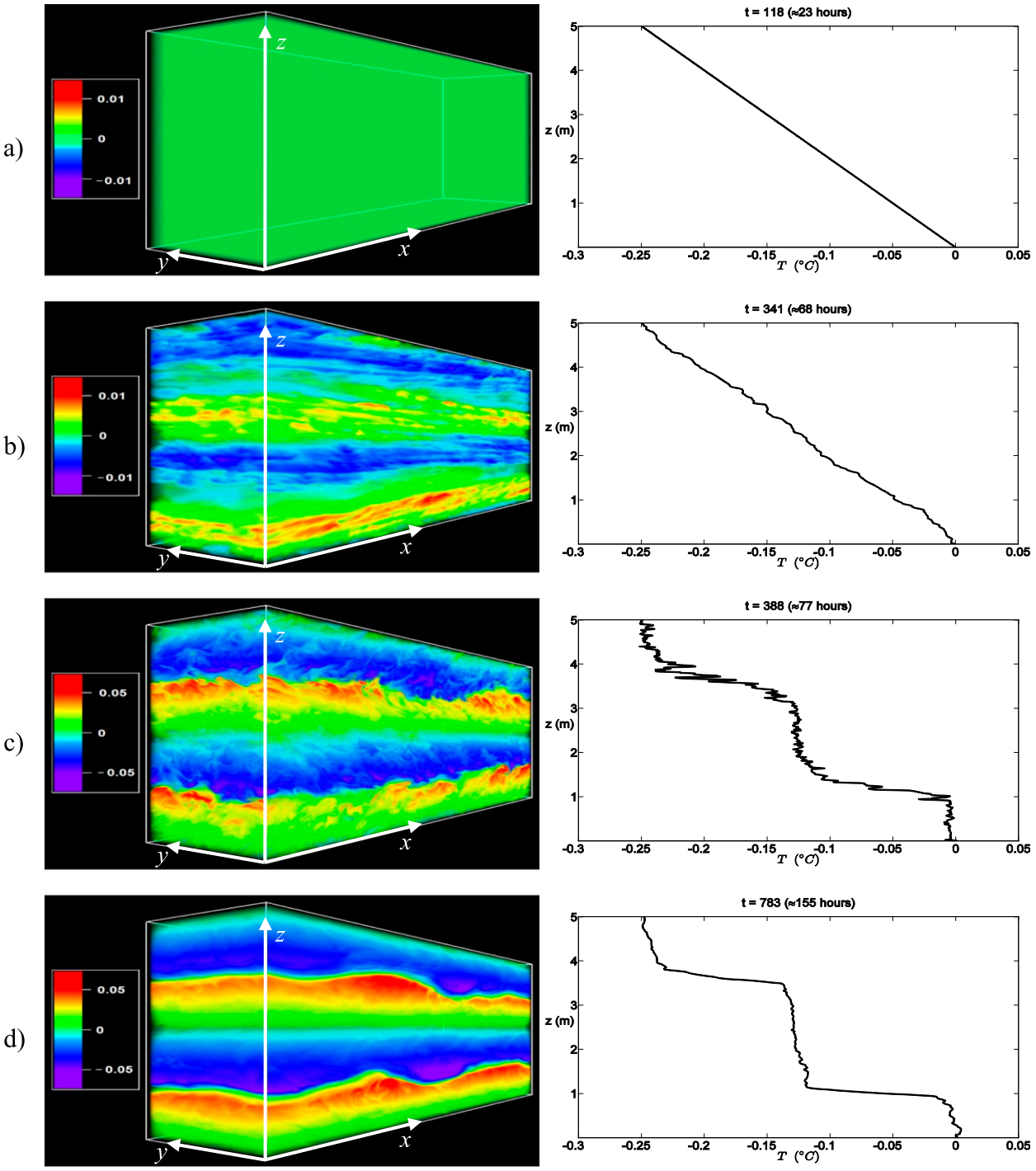

FIG. 7. (left) Dimensional T' and (right) profiles of total temperature T taken from the center ($x = 5$ m, $y = 1.25$ m) of the domain at various times from a 3D DNS with $\tau = 1/3$. (a) The initial fields. (b)–(d) The emergence (≈68 h), merging (≈77 h), and persistence (≈155 h) of layers. Similar dynamics were seen in all 2D and 3D DNS with $\tau < 1$—compare to Figs. 1 and 3.

with $\mathrm{Fr}_{\mathrm{loc}}$ and R_{ρ_loc} from (1) and (2), respectively [and also calculated at the 40-cm (loc) scale]. In (11), the subscript ms denotes derivatives calculated at the grid scale and the overbar denotes averaging over the bin volume. In Fig. 10, we present $\log_{10} k_{T\_\mathrm{loc}}$ and the number of observations in each bin as a function of $\mathrm{Fr}_{\mathrm{loc}}$ and R_{ρ_loc} from both 2D and 3D DNS. For the 2D case, at low R_{ρ_loc} (<1.6), there is lack of variability in

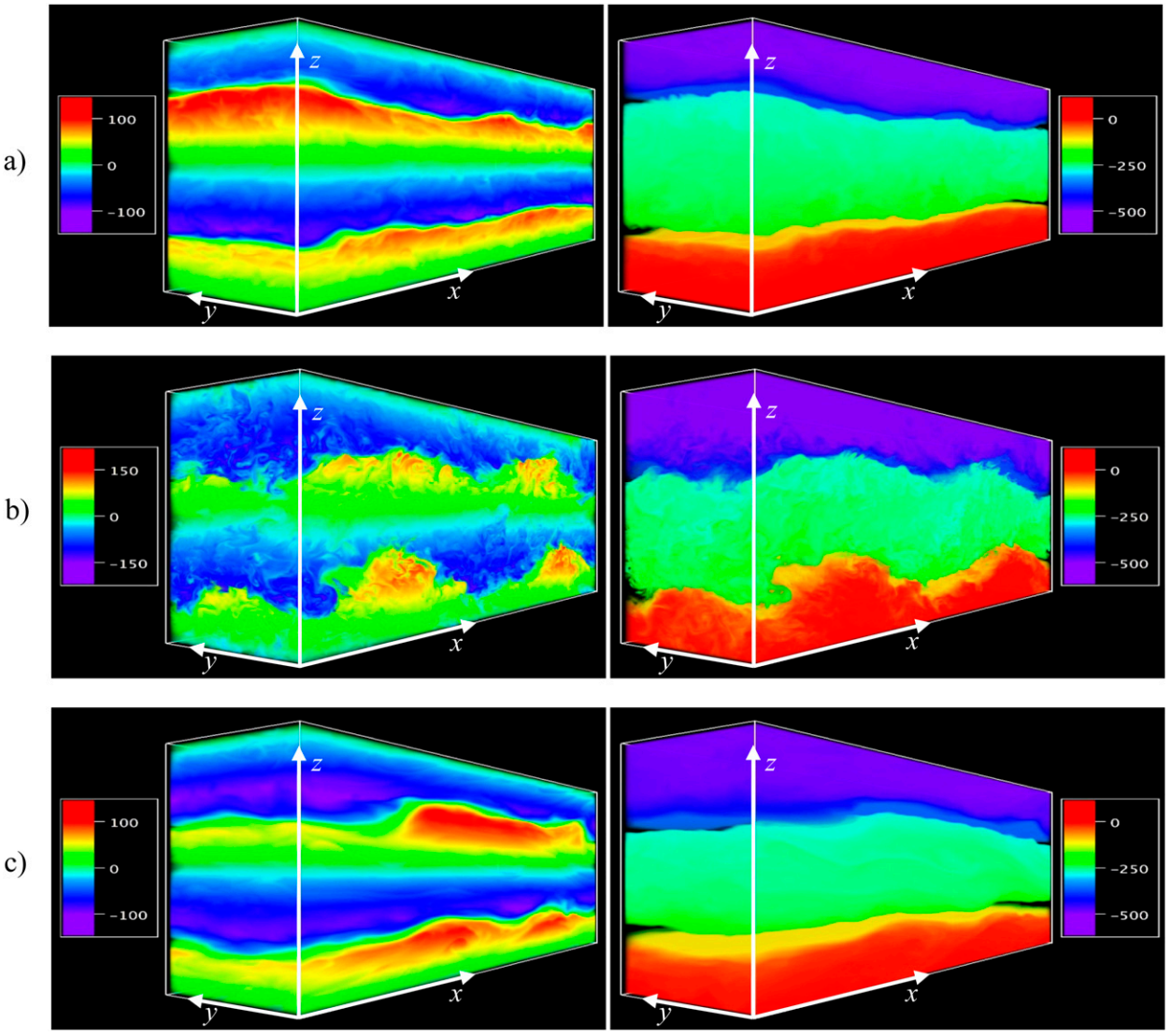

FIG. 8. (left) Nondimensional T' and (right) T fields taken at various times throughout a turbulent event. (a) Well-mixed layers are visible ($t \approx 80$ h) and (b) almost destroyed ($t \approx 83$ h) but (c) quickly reform ($t \approx 87$ h). Both fields are from the 3D DNS described in Fig. 7.

$\log_{10} k_{T\_\mathrm{loc}}$ with respect to $\mathrm{Fr}_{\mathrm{loc}}$, while at high R_{ρ_loc} the dependence is stronger. Dependence on R_{ρ_loc}, particularly at lower $\mathrm{Fr}_{\mathrm{loc}}$, is strong: a decrease in R_{ρ_loc} is associated with a rapid increase in k_{T_loc}. The importance of double diffusion as a driver of thermal diffusivity variance is further verified by consideration of the 3D case. Again, there is strong dependence on R_{ρ_loc} at lower $\mathrm{Fr}_{\mathrm{loc}}$. However, at higher $\mathrm{Fr}_{\mathrm{loc}}$ (>1) there is much stronger variability with $\mathrm{Fr}_{\mathrm{loc}}$. We attribute this to a decrease in the strength of double-diffusive processes—$\tau = \frac{1}{3}$ in 3D as opposed to $\tau = 0.1$ in 2D—and the improved representation of shear-driven turbulence in the 3D DNS.

We have also calculated the bulk quantities according to

$$k_{T\_\mathrm{b}} = \kappa_T \frac{\overline{|\nabla_{\mathrm{ms}} T'|^2}}{(\overline{T}_{z\_\mathrm{b}})^2}, \tag{12}$$

with Fr_b and R_{ρ_b} from (1) and (2), respectively. Here, b derivatives are calculated at the 5-m scale, and the overbar in the numerator of (12) denotes averaging over the domain volume. Figure 11 illustrates the distribution of $\log_{10} k_{T\_b}$ and the number of observations in each bin as a function of Fr_b and R_{ρ_b} from both 2D and 3D DNS. Again there are noticeable differences between the 2D and 3D distributions of $\log_{10} k_{T\_b}$. In 2D, the variability in $\log_{10} k_{T\_b}$ follows a pattern similar to that found at local scales. In 3D, however, variability is dominated by systematic reduction of k_{T_b} with increasing R_{ρ_b}.

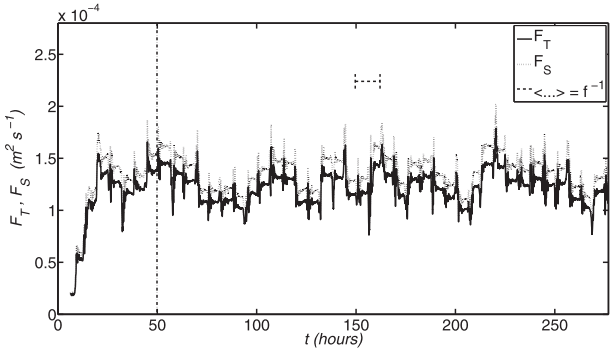

FIG. 9. Representative example of a time series of temperature (solid line) and salinity (dotted line) fluxes calculated over the full domain height (5 m). Boxcar averaging using the period of external forcing (f^{-1}) represented by the dashed line has been used to reduce variability and aid in the determination of flux equilibration (here, $t > 50$ h). Taken from a 2D DNS with $R_\rho = 1.2$, $\tau = 0.1$ and $A = 50$.

There is a clear and important difference between the results shown in Figs. 10 and 11, with the range of $\mathrm{Fr}_{\mathrm{loc}}$ significantly greater than that of Fr_b. The impact of this difference becomes apparent when we attempt a parameterization of k_T and illustrates the need for care when determining the correct choice of outer scale. For instance, in observations of shear-driven turbulence with sensor separation Δz where the probability of low Ri is nonzero, then the correct choice of vertical scale is greater than Δz (Padman and Jones 1985).

4. Parameterization of vertical transport

An important practical outcome of this study is the opportunity to develop convenient, testable, and observationally validated parameterizations for GCMs and large-scale theoretical models. Since finescale shear is usually not captured in numerical climate models, we shall focus on the parameterization of variability in R_ρ.

The parameterization of k_{T_b} was derived from our five 3D DNS and was achieved through consideration of $\langle k_{T\_b} \rangle$, Fr_b, and R_{ρ_b} for each simulation. Each quantity was calculated over the duration for which the system was fully turbulent and $F_{T'}$ and $F_{S'}$ had fully equilibrated.

The parameterization of k_{T_loc} was achieved by first removing all bins with $|T_{z\_\mathrm{loc}}| < 0.001\,^\circ\mathrm{C\,m^{-1}}$, thereby avoiding skewed estimates arising from poorly resolved small vertical gradients. For each bin, the time-mean quantities $\langle k_{T\_\mathrm{loc}} \rangle$, $\langle \mathrm{Fr}_{\mathrm{loc}} \rangle$, and $\langle R_{\rho\_\mathrm{loc}} \rangle$ were calculated over durations 12 h (f^{-1}) in length. These time-mean values were then grouped in five, equal-length $\langle R_{\rho\_\mathrm{loc}} \rangle$ intervals. Within each $\langle R_{\rho\_\mathrm{loc}} \rangle$ interval, an attempt was made to overcome the appearance of large quantities of data at low $\langle \mathrm{Fr}_{\mathrm{loc}} \rangle$ by first grouping $\langle k_{T\_\mathrm{loc}} \rangle$ in equal-length $\langle \mathrm{Fr}_{\mathrm{loc}} \rangle$ subintervals and then calculating $\overline{\langle k_{T\_\mathrm{loc}} \rangle}$ for each. Finally, overall mean values of $\overline{\langle k_{T\_\mathrm{loc}} \rangle}$ for each $\langle R_{\rho\_\mathrm{loc}} \rangle$ interval were found.

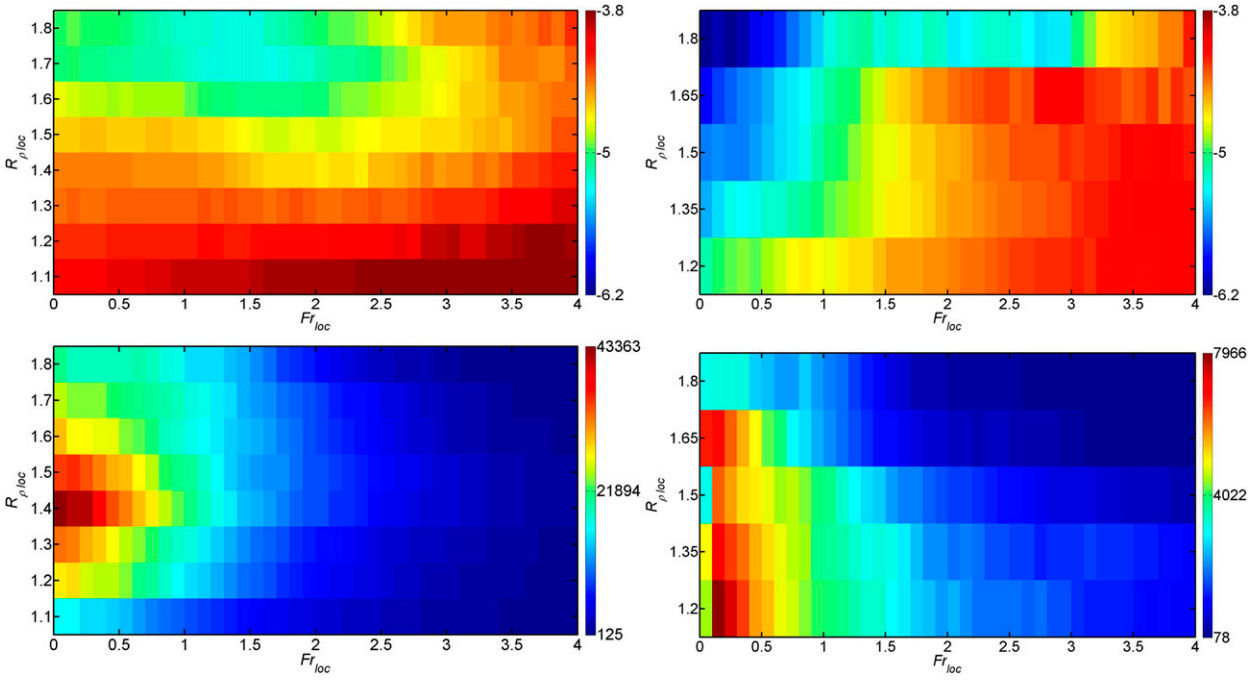

FIG. 10. (top) Estimates of $\log_{10} k_{T\_\mathrm{loc}}$ ($\mathrm{m^2\,s^{-1}}$) as a function of $\mathrm{Fr}_{\mathrm{loc}}$ and R_{ρ_loc} from a series of (left) 2D and (right) 3D DNS. (bottom) The number of data values in each bin.

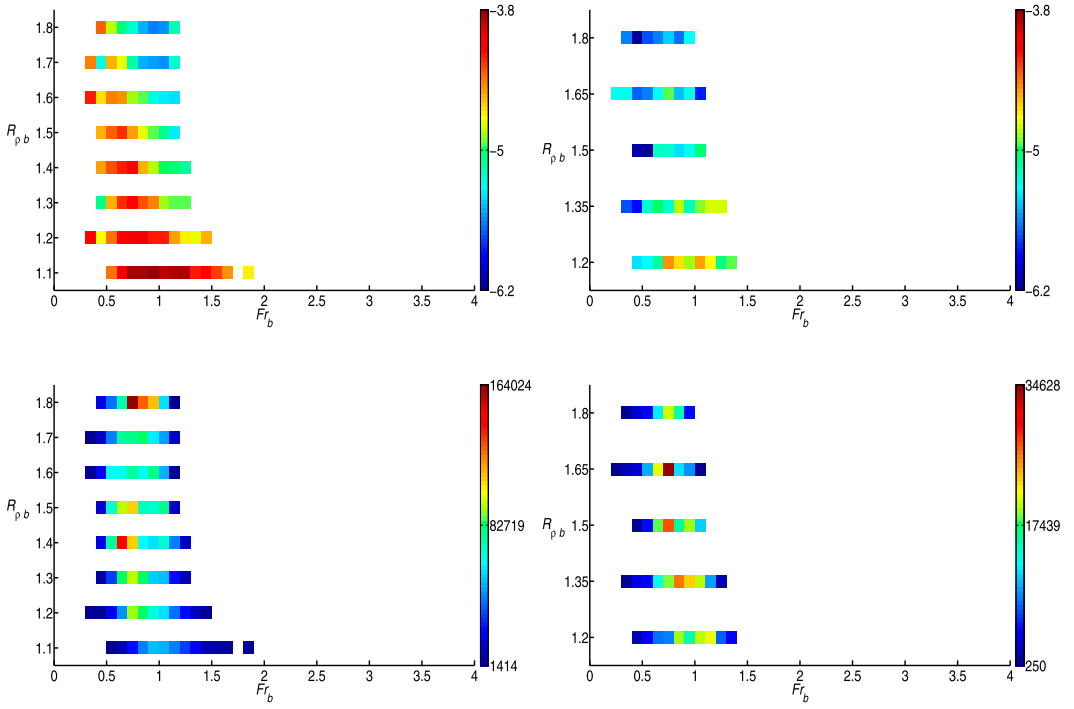

FIG. 11. (top) Estimates of $\log_{10} k_{T\_b}$ ($m^2\,s^{-1}$) as a function of Fr_b and R_{ρ_b} from a series of (left) 2D and(right) 3D DNS. (bottom) The number of data values in each bin.

In each case, a power-law fit of the form

$$k_T = k_0(1 - 1/R_\rho)^{-p} \tag{13}$$

was sought, varying both k_0 and p. The form of (13) was chosen since $R_\rho = 1$ is the threshold between statically stable and statically unstable regimes, with fluxes expected to increase dramatically as $R_\rho \to 1^+$. Additionally, such a form has been physically justified and successfully tested (Radko 2008; Radko and Smith 2012) for the salt finger regime. The parameterization based on outer scales yields $k_0 = 2.6 \times 10^{-6}\,m^2\,s^{-1}$, $p = 1.67$, and is one of the main findings of this study. By comparison, the parameterization based on local scales yields $k_0 = 4.12 \times 10^{-5}\,m^2\,s^{-1}$ and $p = 0.47$.

The goodness of each fit is given in Table 1 where it can be seen, from the higher R^2 and lower RMSE, that the fit based on outer scales produces least error. The fit (13) was derived based on dissipation. Analogous calculations based on fluxes slightly raise the outer scales exponent to 1.69. This difference is ultimately due to errors in the Osborn–Cox relation (see section 5). In Table 2, we present the (nondimensional and dimensional) volume-averaged temperature flux $\langle F_{T\_b} \rangle$ as well as $\langle k_{T\_b} \rangle$ found using (12) and $\kappa_T \langle F_{T\_b} \rangle$ for each 3D DNS.

The results of this fitting procedure and the values $\langle k_{T\_b} \rangle$ and $\langle k_{T\_\mathrm{loc}} \rangle$ found from our DNS are shown in Fig. 12. Also shown in Fig. 12 is the best fit found in Part I (also based on outer scales), where $k_0 = 3.9 \times 10^{-6}\,m^2\,s^{-1}$ and $p = 1.5$, both of which fall within the 95% confidence intervals for k_{T_b} (Table 1) and well outside those for k_{T_loc}. The variability of k_{T_b} with Fr is illustrated in Fig. 12 by the outer-scale fit found for $\mathrm{Fr} < 0.7$. The agreement between this fit and that found for $\mathrm{Fr} > 0$ is close, particularly at large R_ρ. For the $\mathrm{Fr} < 0.7$ fit, the exponent p has reduced to 1.1 with little change in k_0. The close agreement between our outer scales fit and the fit from Part I gives us confidence that our model is in fact representative of conditions described in Part I.

TABLE 1. A summary of goodness of fit data (confidence interval, C.I.) for the R_ρ parameterization of k_T based on 40-cm (k_{T_loc}) and 5-m (k_{T_b}) scales.

Fit type	95% C.I. for p	95% C.I. for k_0	R − square	RMSE
k_{T_loc}	[−0.008, 0.946]	$[1.42, 6.82] \times 10^{-5}$	0.7564	9.19×10^{-6}
k_{T_b}	[1.229, 2.110]	$[0.72, 4.47] \times 10^{-6}$	0.9840	2.53×10^{-6}

TABLE 2. A summary of data diagnosed for a series of 3D DNS. Row one shows $\langle k_{T\_b} \rangle$ as calculated from (12). Row two shows nondimensional $\langle F_{T\_b} \rangle$. Row three shows dimensional $\langle F^*_{T\_b} \rangle$, denoted by the asterisk. Row four shows the dimensional quantity $\langle k_{T\_b} \rangle = \kappa_T \langle F_{T\_b} \rangle$.

R_ρ	1.2	1.35	1.5	1.65	1.8
$\langle k_{T\_b} \rangle (\mathrm{m^2\,s^{-1}})$	5.2×10^{-5}	2.4×10^{-5}	2.0×10^{-5}	1.1×10^{-5}	0.8×10^{-5}
$\langle F_{T\_b} \rangle$	394.6	179.5	155.5	83.4	67.2
$\langle F^*_{T\_b} \rangle (^\circ\mathrm{C\,m\,s^{-1}})$	2.8×10^{-6}	1.3×10^{-6}	1.1×10^{-6}	0.6×10^{-6}	0.5×10^{-6}
$\kappa_T \langle F_{T\_b} \rangle (\mathrm{m^2\,s^{-1}})$	5.5×10^{-5}	2.5×10^{-5}	2.1×10^{-5}	1.1×10^{-5}	0.9×10^{-5}

One of the most commonly used characteristics of double-diffusive flows is the flux ratio ($\gamma = F_S/F_T$), which we estimate from equilibrated fluxes of temperature and salinity recorded during the series of 3D DNS. For all values of R_ρ, strong variation in A (shearing force amplitude) results in weak variation in γ. For example, for the 2D case where $R_\rho = 1.2$ (section 2) increasing A from 35 to 100 resulted in a 4.4% increase in γ. Thus, it is reasonable to consider dependence of γ on R_ρ only. Figure 13 presents the numerical estimates of γ [based on the "outer" (5 m) scale] as a function of R_ρ and a linear best fit that takes the form

$$\gamma = 0.52 R_\rho + 0.53. \tag{14}$$

Also shown in Fig. 13 is the line $\gamma = R_\rho$ (expected when double diffusion is not active) and the monotonically decreasing parameterization $\gamma_{\mathrm{Kelley}} = [R_\rho + 1.4(R_\rho - 1)^{3/2}]/[1 + 14(R_\rho - 1)^{3/2}]$ from Kelley (1990). The effect of turbulence is evidenced by an increase from γ_{Kelley} toward $\gamma = R_\rho$ for all $R_\rho > 1$—an effect that is also reported by Canuto et al. (2008) and for the salt finger case by Wells and Griffiths (2003). Because of the different monotonicities of the two relations, the relative increase in the flux ratio is much greater at higher R_ρ (not shown).

Equations (13) and (14), in combination with the relation $k_S = k_T \gamma R_\rho^{-1}$, leads to the outer (5 m) scale parameterization:

$$k_S = k_0 (0.52 + 0.53 R_\rho^{-1})(1 - R_\rho^{-1})^{-p}, \tag{15}$$

where $k_0 = 2.6 \times 10^{-6}\,\mathrm{m^2\,s^{-1}}$ and $p = 1.67$. Equation (15) represents a parameterization for the diffusivity of salt that is otherwise inaccessible from observations. In conjunction with (13), it is one of the primary findings of this study, an aim of which is to provide a parameterization that can be utilized in coarse-resolution GCMs where only the "outer scales" are available.

The 3D DNS conducted here are for the case where $\tau = 1/3$, which can lead to concerns regarding the accuracy of (15). However, based on the analysis of various finite τ (e.g., see section 2), salinity fluxes do converge in the limit $\tau \to 0$ (relevant to the ocean), and even DNS with $\tau = 1/3$ offer an adequate estimate of the salinity flux, with differences of ~2% to those with $\tau = 0.1$. In Fig. 14a, we plot the outer-scale parameterization of k_T [(13)] and k_S [(15)] as well as those of Kelley (1984), while in Figs. 14b and 14c we plot the ratios $k_T/k_{T\_\mathrm{Kelley}}$ and $k_S/k_{S\_\mathrm{Kelley}}$, respectively. At lowest values of R_ρ (< 1.1), both k_T and k_S are significantly higher than k_{T_Kelley} and k_{S_Kelley}, an effect that can be directly attributed to the singularity in (13) and (15) as $R_\rho \to 1^+$. For all other values of R_ρ, there is an approximate factor of 2 difference between k_T and k_{T_Kelley}, with k_T lower for $1.2 < R_\rho < 3.4$ and higher otherwise. There is good agreement between k_S and k_{S_Kelley} for $1.1 < R_\rho < 1.8$, with k_S higher by less than a factor of 2. The discontinuity at $R_\rho = 2$ in Fig. 14c is a direct consequence of the use of a piecewise parameterization in Kelley (1984). As R_ρ is increased from 1.8, the agreement between k_S and k_{S_Kelley} lessens, with the ratio having a maximum value of 64 at $R_\rho = 10$. We attribute this disparity to the differences in flux ratio parameterization discussed above and seen in Fig. 13.

While the current formulation takes into account only density ratio effects, for future generations of ocean models, capable of representing finescale shears,

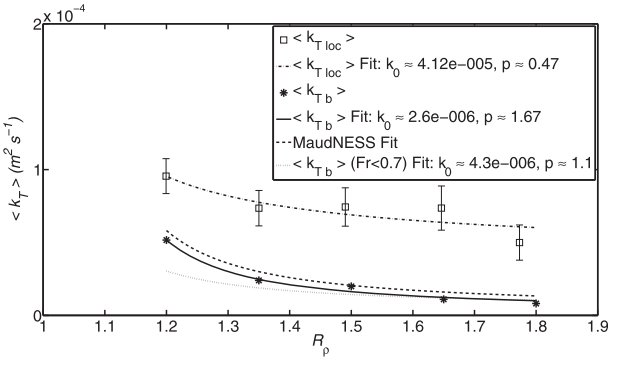

FIG. 12. The 3D DNS k_T parameterizations based on local (subscript loc) and outer (subscript b) scales. At local scales (squares with error bars and dashed–dotted line) k_T is overestimated by as much as a factor of 6. At outer scales (asterisks and solid line), there is strong agreement with the parameterization found in Part I (dashed line). Also shown (dotted line) is the parameterization found for small Fr.

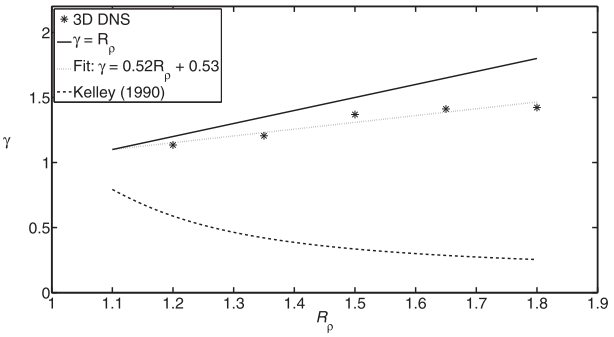

FIG. 13. The 3D DNS estimates (asterisks) of flux ratio γ and a linear best fit (dotted line) of the form: $\gamma = 0.52R_\rho + 0.53$. Also shown is the (solid) line $\gamma = R_\rho$, expected when double diffusion is not active and (dashed line) the parameterization of Kelley (1990).

parameterizations should include dependencies on both R_ρ and outer Fr.

5. Applicability of the thermal production–dissipation and TKE balances

a. *Production–dissipation*

For consistency, we have followed the procedures adopted in Part I. There, thermal diffusivity was estimated using the method of Osborn and Cox (1972) in which a balance is assumed between the production and dissipation of turbulent temperature variance χ_T. Since we have access to more complete recordings of vertical fluxes of temperature from our 3D DNS, an opportunity arose to test the assumed balance between temperature fluxes and the thermal dissipation rate. Previous studies have shown that excluding terms in the budget of turbulent thermal variance can lead to inaccurate estimates of χ_T, for example, lateral gradients (Gregg 1987) and accumulation terms (Davis 1994). In what follows, we address the question of which terms contribute most error. Our results show that estimates of thermal diffusivity based on χ_T can vary significantly according to the time-averaging period utilized. At the instantaneous level, the magnitude of (nondimensional) dissipation is considerably different than that of vertical flux, which in turn can lead to inaccurate estimation of k_T. However, when time-averaged dissipation is utilized, the discrepancy lessens for longer averaging periods. An example of this effect is presented in Fig. 15, where we plot (from a 3D DNS with $R_\rho = 1.2$ and $\tau = 1/3$) a time series of the ratio of temperature flux to dissipation, calculated both instantaneously and when averaged over the period of the external forcing. Nonaveraged values have a mean value of 3.84 and maximum of 105, while averaged values have a mean of 1.07 and a maximum of 1.34, lending support to the hypothesis that the

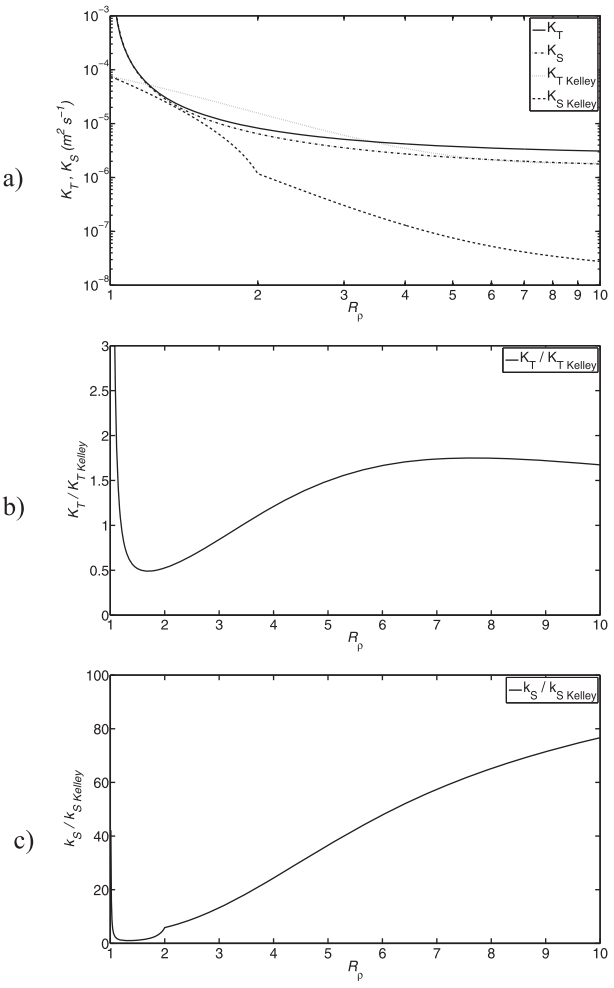

FIG. 14. (a) The outer-scale parameterizations (13) and (15) alongside those of Kelley (1984). (b),(c) Also shown are their respective ratios.

assumption of a balance between production and dissipation strengthens for longer averaging time scales. We have calculated the associated error from the formula $\text{err} = [(\langle F_T \rangle_{T_{\text{avg}}} / \langle \chi_T \rangle_{T_{\text{avg}}} - 1)^2]^{1/2}$, where T_{avg} is the averaging period. Also shown in Fig. 15 is the error as a function of T_{avg}/f^{-1}. The error quickly decreases from the instantaneous value (~1300%) to ~200% at $T_{\text{avg}}/f^{-1} \sim 0.25$—an interval of ~3 h—and continues to decrease to ≈10% when averaging extends to cover a forcing period. By comparison, at intervals corresponding to the buoyancy period ($T_b \sim 0.7$ h), the error is 650%. Therefore, for sufficient accuracy, averaging intervals on the order $T_{\text{avg}} \gg T_b$ should be considered.

We have also examined the effect of a decrease in the horizontal length scale L_{avg} over which F_T and χ_T are calculated. For comparison with results in Fig. 15, we have utilized the 3D DNS with $R_\rho = 1.2$ and $\tau = 1/3$. Beginning at $L_{\text{avg}} = 5$ m, the domain was partitioned into

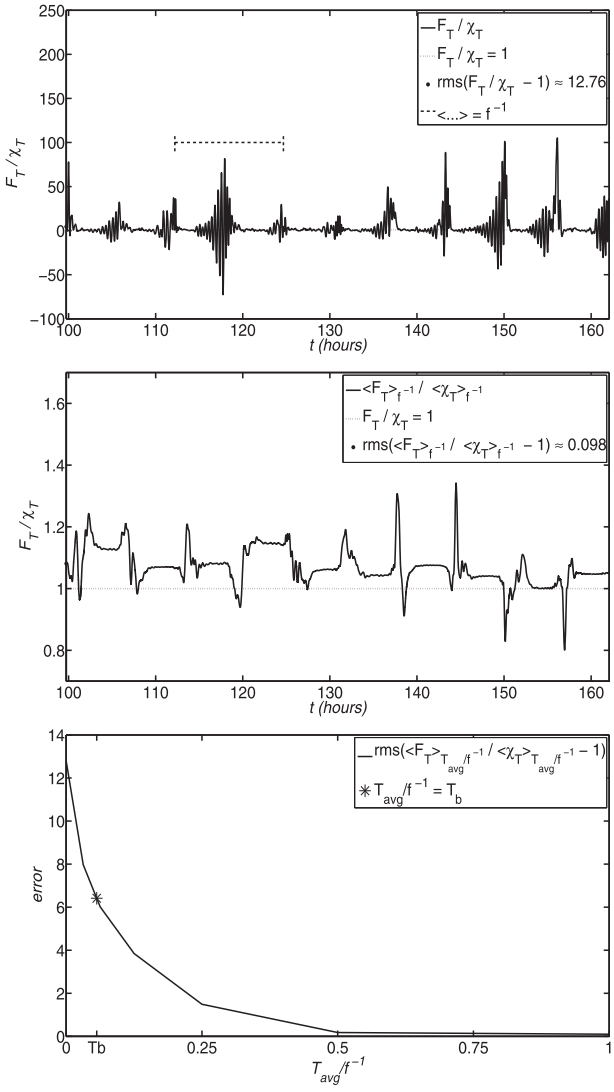

FIG. 15. (top) The ratio of temperature flux and dissipation (solid line) when calculated at the instantaneous level giving an error $\approx 1300\%$ [calculated from rms$(F_T/\chi_T - 1)$]. Also shown are (dotted line) the zero error value $F_T/\chi_T = 1$ and (dashed line) the interval f^{-1} corresponding to the period of external forcing. (middle) The ratio of temperature flux and dissipation when time averaging over the interval f^{-1} has been applied. The error has dropped to $\sim 10\%$. (bottom) The effect of increasing the averaging interval from 0 to f^{-1}. The error drops to $\approx 650\%$ when $T_{\rm avg}/f^{-1}$ is equal to the buoyancy period ($T_b = 2\pi/N \approx 0.7$ h) to $\approx 200\%$ when $T_{\rm avg}/f^{-1} \sim 0.25$, corresponding to an averaging interval of ~ 3 h. Taken from the 3D DNS with $R_\rho = 1.2$ and $\tau = 1/3$.

$n = 10\,{\rm m}/L_{\rm avg}$ subdomains of size $L_{\rm avg} \times 2.5\,{\rm m} \times 2.5\,{\rm m}$ and the quantities F_T^i and χ_T^i $(i = 1 \ldots n)$ were recorded for each of the n partitions. Once time-averaging had been applied (utilizing $T_{\rm avg}/f^{-1} = 1$), the quantities ${\rm err}_i = [(\langle F_T^i\rangle/\langle\chi_T^i\rangle - 1)^2]^{1/2}$ were calculated and then averaged to give the relative error. From Fig. 16, the error increases monotonically to $\sim 140\%$ as $L_{\rm avg} \to 0^+$—a full

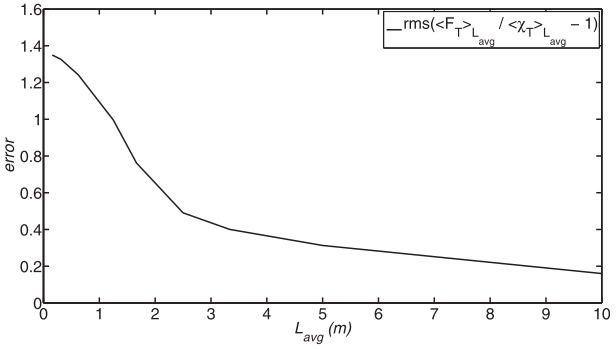

FIG. 16. The relative error in the Osborn and Cox (1972) model resulting from changes in the horizontal length scale $L_{\rm avg}$ over which F_T and χ_T are calculated. Throughout, the averaging period $T_{\rm avg}$ is maintained at the period of shear forcing f^{-1} so that the error at $L_{\rm avg} = 10$ m coincides with that at $T_{\rm avg}/f^{-1} = 1$ in Fig. 15 (bottom panel). Taken from the 3D DNS with $R_\rho = 1.2$ and $\tau = 1/3$.

order of magnitude less than that seen in Fig. 15 (bottom panel) when $T_{\rm avg}/f^{-1} \to 0$. We interpret this result as evidence that inaccuracies in the Osborn and Cox (1972) model, for the setup in this study, are primarily associated with the (temporal) accumulation term in the thermal variance budget.

b. TKE

Following Osborn (1980), the TKE budget is written as $B + \varepsilon = P$, expressing a balance between buoyancy flux

$$B = \frac{g}{\rho_0}\overline{w'\rho'}, \tag{16}$$

molecular dissipation ε, and energy production P. The three-way balance can be expressed using either the flux Richardson number $R_f = B/P = B/(B + \varepsilon)$ or the efficiency factor

$$\Gamma_e = \frac{R_f}{1 - R_f} = \frac{B}{\varepsilon}, \tag{17}$$

describing the ratio of potential energy gain to kinetic energy loss.

We have calculated this quantity both exactly and under the assumption of isotropy (subscript iso) using

$$\varepsilon = \frac{\nu}{2}\overline{\left(\frac{\partial u_i'}{\partial x_j} + \frac{\partial u_j'}{\partial x_i}\right)^2} \tag{18}$$

and

$$\varepsilon_{\rm iso} = \frac{15\nu}{4}(\overline{u_z'^2} + \overline{v_z'^2}). \tag{19}$$

Another commonly used quantity is the dissipation ratio calculated from

TABLE 3. A comparison of χ_T and ε calculated both with the assumption of isotropy (subscript iso) and without for a series of 3D DNS where double diffusion is active ($\tau = 1/3$) and inactive ($\tau = 1$).

	$R_\rho = 1.2$ ($\tau = 1/3$)	$R_\rho = 1.5$ ($\tau = 1/3$)	$R_\rho = 1.8$ ($\tau = 1/3$)	$R_\rho = 1.2$ ($\tau = 1$)
χ_T ($m^2\,s^{-1}$)	1.11×10^{-4}	4.22×10^{-5}	1.78×10^{-5}	9.72×10^{-5}
ε ($m^2\,s^{-1}$)	5.93×10^{-4}	6.13×10^{-4}	5.93×10^{-4}	6.03×10^{-4}
χ_{T_iso} ($m^2\,s^{-1}$)	1.14×10^{-4}	5.18×10^{-5}	2.53×10^{-5}	1.05×10^{-4}
ε_{iso} ($m^2\,s^{-1}$)	6.72×10^{-4}	7.57×10^{-4}	7.69×10^{-4}	7.18×10^{-4}

$$\Gamma = \frac{\chi_T N^2}{2\varepsilon \overline{T}_z^2}. \tag{20}$$

For consistency, we have calculated this quantity both exactly and under the assumption of isotropy using

$$\chi_T = 2\kappa_T \overline{\left(\frac{\partial T'}{\partial x_i}\right)^2}, \tag{21}$$

and

$$\chi_{T\_iso} = 6\kappa_T \overline{\left(\frac{\partial T'}{\partial z}\right)^2}. \tag{22}$$

Previous studies have shown that when isotropic formulas are used, estimates of ε and χ_T can be inaccurate. For instance, Itsweire et al. (1993) showed, through DNS of stably stratified turbulent shear flows, that the error introduced can be up to a factor of 4. Caplan (2008) utilized salt-finger DNS to show that isotropic estimates could lead to error factors as high as 1.3 and 2 in χ_T and ε, respectively. Kimura et al. (2011) extended the salt finger analysis to include a sheared background flow and found little change to the results of Caplan.

To test the applicability of these findings to our diffusive convection setup, we have calculated the quantities (18)–(19) and (21)–(22) for the 3D DNS with $\tau = 1/3$, $R_\rho = 1.2$, 1.5, 1.8, and also for a 3D ($R_\rho = 1.2$) DNS identical in every respect to that where $\tau = 1/3$, but with $\tau = 1$. The results of these calculations are shown in Table 3. A comparison of χ_T and χ_{T_iso} reveals differences from as low as 3% ($R_\rho = 1.2$) up to 42% ($R_\rho = 1.8$) for the double-diffusive case and ~8% in the non-double-diffusive case. A similar comparison of ε and ε_{iso} reveals differences of 12%–23% for all three double-diffusive cases and ~16% for the non-double-diffusive case. From these calculations, we conclude that estimates based on the isotropy assumption are less accurate where microstructure is double diffusive in origin, particularly at large R_ρ, where χ_{T_iso} introduces discrepancies that are 2–3 times larger than in the case of mechanically generated microstructure. In Table 4, we tabulate the relative contribution of each term in (18) and (21). For low R_ρ calculations of χ_T, the combined contribution of lateral temperature gradients roughly balance that of vertical temperature gradients, resulting in minimal error in the assumption of isotropy. However, as R_ρ is increased, this balance no longer holds, with the contribution from lateral gradients becoming less, relative to that of vertical gradients. For calculations of ε, the picture is much less clear and the error is a result of several discrepancies. For example, isotropy assumes equal contributions from the terms $2(u'_x)^2$, $(u'_y)^2$, and $(u'_z)^2$ that is clearly not the case, particularly for large R_ρ. Further discrepancies, albeit to a lesser degree, can be seen for the two similar sets of terms involving the velocity components v and w as well as those involving mixed components. Finally the assumption that vertical shear in the x and y directions are balanced $[(u'_z)^2 = (v'_z)^2]$ is questionable, particularly at large R_ρ.

As seen in section 2, the differences between the two regimes (double-diffusive and non-double-diffusive cases) are made clear by the comparison of density fluxes $F_{\rho'}$—further evidenced in Fig. 17 where we plot thermal, salt, and buoyancy diffusivities from the 3D DNS with $\tau = 1$ and $\tau = 1/3$ with $R_\rho = 1.2$. There is slight increase (2.5%) in $\langle k_T \rangle$ as τ is increased but a much larger

TABLE 4. The mean relative contribution of each term to the calculation of (rows 2–4) χ_T and (rows 5–16) ε according to (21) and (18), respectively.

	$R_\rho = 1.2$ ($\tau = 1/3$)	$R_\rho = 1.5$ ($\tau = 1/3$)	$R_\rho = 1.8$ ($\tau = 1/3$)	$R_\rho = 1.2$ ($\tau = 1$)
$(T'_x)^2$	0.26	0.20	0.15	0.25
$(T'_y)^2$	0.30	0.24	0.19	0.29
$(T'_z)^2$	0.44	0.56	0.67	0.46
$2(u'_x)^2$	0.11	0.10	0.09	0.11
$(u'_y)^2$	0.12	0.12	0.12	0.13
$(u'_z)^2$	0.21	0.28	0.31	0.23
$(v'_x)^2$	0.09	0.08	0.08	0.09
$2(v'_y)^2$	0.12	0.11	0.11	0.12
$(v'_z)^2$	0.14	0.15	0.14	0.15
$(w'_x)^2$	0.11	0.09	0.08	0.10
$(w'_y)^2$	0.14	0.12	0.11	0.12
$2(w'_z)^2$	0.14	0.14	0.12	0.13
$2u'_y v'_x$	−0.05	−0.04	−0.04	−0.05
$2u'_z w'_x$	−0.06	−0.06	−0.05	−0.06
$2v'_z w'_y$	−0.08	−0.07	−0.07	−0.07

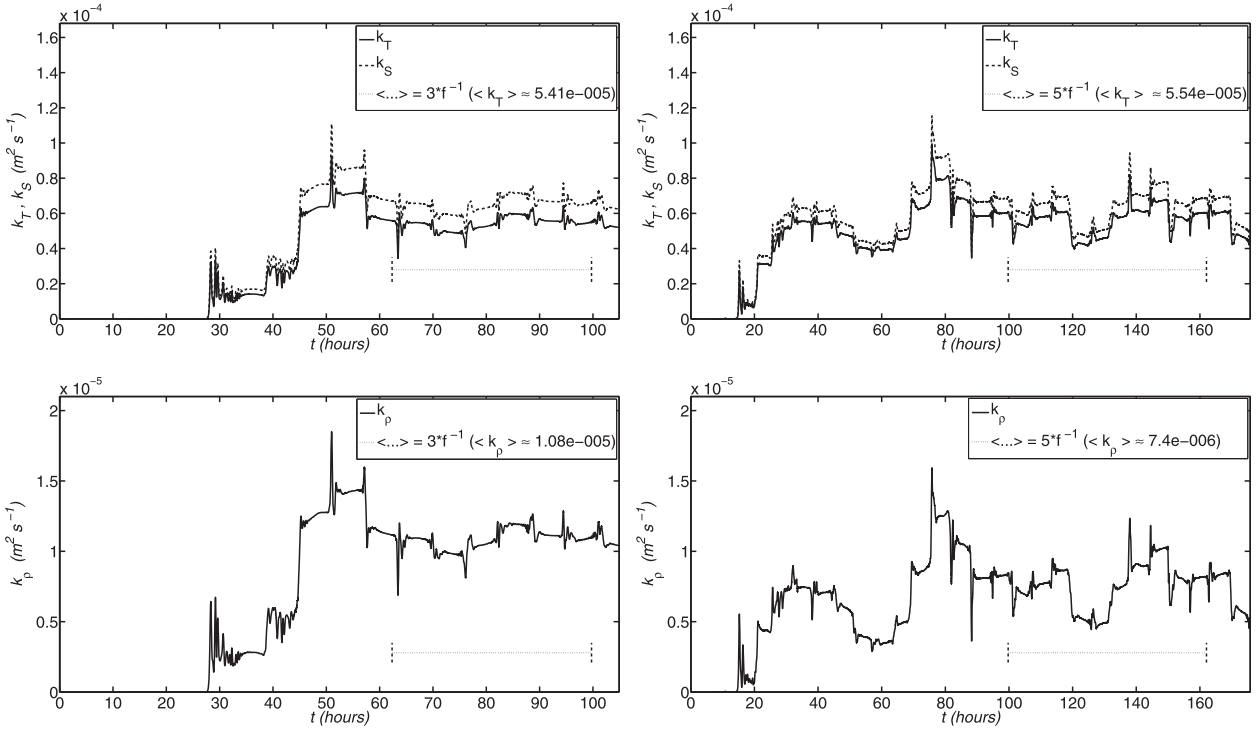

FIG. 17. (top) Estimates of k_T, k_S, and (bottom) k_ρ from two 3D DNS—one with (left) $\tau = 1$ (no double diffusion) and the other with (right) $\tau = 1/3$. Also shown (dashed lines) are the intervals over which average values have been calculated. There is a slight increase in k_T as τ is decreased, but a much larger (relative) decrease in k_ρ reflecting the tendency of double diffusion to transport density in the upgradient sense.

decrease (31.3%) in $\langle k_\rho \rangle$. As pointed out in section 2, it should be expected that decreasing τ toward more realistic values would greatly enhance this effect, the ramifications of which are made clear by consideration of Γ_e and Γ.

In purely turbulent flows, it is expected that $\Gamma = \Gamma_e$. Our 3D DNS have given an additional opportunity to test this assumption both in the non-double-diffusive and double-diffusive regimes. The results of these calculations are shown in Table 5. In the non-double-diffusive regime, $\Gamma \approx \Gamma_e$ as expected, with $\Gamma/\Gamma_e \approx 0.9$ and $\Gamma_{\rm iso}/\Gamma_{e\_{\rm iso}} \approx 0.98$. However, when double diffusion is included, $1.24 < \Gamma/\Gamma_e < 1.43$ and $1.44 < \Gamma_{\rm iso}/\Gamma_{e\_{\rm iso}} < 2.15$. In pure double diffusion, diffusive convection is driven by the release of potential energy from the temperature stratification, and shear production is thought to be inconsequential. As $P \to 0$, the TKE balance reduces to the simple equation $B = -\varepsilon$, and therefore $\Gamma_e = -1$. For the double-diffusive case where $R_\rho = 1.2$ and $\tau = 1/3$, Γ_e and $\Gamma_{e\_{\rm iso}}$ are 26% and 23% less, respectively, than those values found when $\tau = 1$. Given that frictional loss of energy is higher for turbulent flows than for double-diffusive flows, it is expected that Γ should be higher for the latter regime. For instance, both St. Laurent and Schmitt (1999) and Canuto et al. (2008) report values up to 0.6 where salt fingering is strong and shear is weak, while Oakey (1988) reports even higher values found through analysis of data from Meddy Sharon. Inspection of the values found for $R_\rho = 1.2$ and $\tau = 1/3$ reveal that Γ and $\Gamma_{\rm iso}$ are 14% and 16% higher, respectively, than those values found when $\tau = 1$. We interpret the reductions in Γ_e and $\Gamma_{e\_{\rm iso}}$ and the increases in Γ and $\Gamma_{\rm iso}$ to be suggestive of microstructure that is double diffusive in origin. Here, we have examined the weak case $\tau = 1/3$ and would expect Γ_e, $\Gamma_{e\_{\rm iso}} \to -1$ and Γ, $\Gamma_{\rm iso} \to 1$ as $\tau \to 0$.

TABLE 5. A comparison of dissipation ratio Γ and efficiency factor Γ_e, both with the assumptions of isotropy (subscript iso) and without for a series of 3D DNS where double diffusion is active ($\tau = 1/3$) and inactive ($\tau = 1$).

	$R_\rho = 1.2$ ($\tau = 1/3$)	$R_\rho = 1.5$ ($\tau = 1/3$)	$R_\rho = 1.8$ ($\tau = 1/3$)	$R_\rho = 1.2$ ($\tau = 1$)
Γ	0.235	0.234	0.145	0.207
Γ_e	0.169	0.189	0.102	0.230
$\Gamma_{\rm iso}$	0.218	0.220	0.170	0.189
$\Gamma_{e\_{\rm iso}}$	0.149	0.153	0.079	0.193

6. Conclusions

This study has been motivated by a series of observations taken during the 2005 MaudNESS expedition to the eastern Weddell Sea, the purpose of which was to provide insight into the stability of the water column in that region. Subsequent data analysis conducted by the participants of that expedition, as detailed in Part I, revealed a strong dependence of thermal diffusivity on density ratio and provided a parameterization reflecting this dependence.

We have advanced our understanding of the interaction of dynamic and double-diffusive instabilities for parameters relevant for MaudNESS conditions through the following:

1) The dynamics and mixing characteristics observed in the Weddell Sea have been explained using a simple model that incorporates a linear equation of state, fixed-amplitude oscillatory forcing, and double-diffusive dynamics.
2) Estimates of k_T based on the maximum spatial and temporal scales permitted by our DNS differ substantially from those found using local scales.
3) The parameterization of k_T reported in Part I has been replicated and supplemented further through a parameterization of k_S that is inaccessible in the observational data.
4) We have examined the applicability of thermal production–dissipation balance, commonly assumed in microstructure analysis, and quantified the averaging period required for accuracy, that is, much greater than the buoyancy period. Additional calculations with varying length scales suggest that the error in the Osborn and Cox (1972) relation is primarily due to the assumption that the accumulation term is negligible.
5) We have also examined the TKE balance for both the double-diffusive and non-double-diffusive cases. Analyses of Γ and Γ_e reveal that the relation $\Gamma = \Gamma_e$ holds for the non-double-diffusive regime, but significant revision is required when double diffusion is active.
6) The importance of double diffusion as a mixing process has been further illustrated by the comparison of density fluxes and γ from DNS in which diffusive convection is either active or inactive, with both quantities showing significant differences.
7) Our results have shown instances of instability arising in the regime of high (minimum) Richardson number—greater than 0.4—and diffusive convection, thus providing evidence that double diffusion could be responsible for the destabilization of laminar finescale flows where $\mathrm{Ri} > 1/4$, a hypothesis postulated for the salt finger case by Radko and Stern (2011).
8) The isotropy assumption for the dissipation of thermal variance χ_T and TKE ε has been tested and shown to be responsible for maximum diagnostic error of 42% and 23%, respectively, where double diffusion is active. Errors of 8% and 16% are found where double diffusion is not active.

Cabbeling effects, which are a direct result of nonlinearities in the equation of state, are absent from our model. Therefore, it is reasonable to conclude, given the similarities between our results and those of Part I, that observations are sufficiently explained by double diffusion. Likewise, most of our solutions (particularly 3D) employed τ that is much higher than realized in the ocean. In view of these findings, we expect the impact of double diffusion in the real ocean to be even more profound.

Acknowledgments. This work was supported by NSF Grant ANT-0944536. This research was performed while the first author Flanagan held a National Research Council Award at the Naval Postgraduate School, Monterey. This work used the Extreme Science and Engineering Discovery Environment (XSEDE), which is supported by National Science Foundation Grant Number ACI-1053575. The authors thank Eric Kunze, Laurie Padman, and two anonymous reviewers for their many valuable comments and suggestions.

APPENDIX

Instability of High Ri Flows

As seen in Figs. 1, 3, 7, and 8, layer formation and their subsequent merging are predominant characteristics in the evolution of the system. Questions naturally arise as to the effects of an increase or decrease in the amplitude of the shearing force A. We have attempted to answer this question through an examination of 2D DNS. For all cases where A was increased beyond A_{cr}, so that $\mathrm{Ri} < 1/4$ for greater fractions of the shear period, layer formation continued to occur but at earlier times, with K–H instability dominating at sufficiently large A (e.g., when $A = 100$ and $R_\rho = 1.2$, not shown). Of great interest is the case where A is decreased sufficiently so that shear remains subcritical. From classical theory (Richardson 1920; Miles 1961; Howard 1961) the requirement for instability is that Ri be less than $\frac{1}{4}$. To test this requirement, a series of DNS were conducted, whereby A was reduced from 50 with $R_\rho = 1.5$, $\mathrm{Pr} = 13$, and $\tau = 0.1$. Example plots of T' are given in Fig. A1 for the case where $A = 35$. From (10), $A_{\mathrm{cr}} = 40.6$, and our

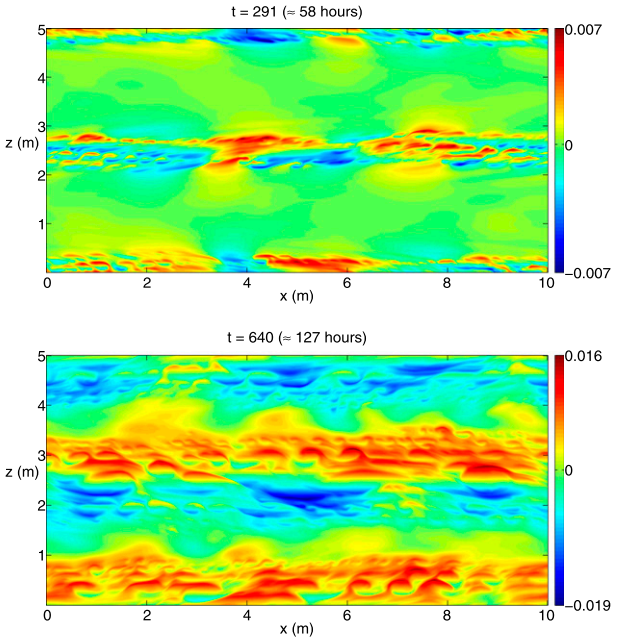

FIG. A1. Temperature perturbation fields at different times: (top) $t \approx 58$ h and (bottom) $t \approx 127$ h. From the 2D DNS with $R_\rho = 1.5$, $\tau = 0.1$ and $A = 35$ ($A_{cr} = 40.6$). Here, min(Ri) = 0.4237. However, dynamic instability is visible at various times throughout the experiment.

setup implies that the Richardson criterion is not met—in fact, min(Ri) $\cong$ 0.424 for the initial sinusoidal pattern. Surprisingly, dynamic instability is readily observed both at the initial stages of layer formation and later in the run, even though min(Ri) $> 1/4$. Although not as obvious as that presented in Fig. A1, traces of such instability were also visible for min(Ri) $\cong$ 0.457 ($A = 30$, not shown). Similar effects have been reported by Radko and Stern (2011) for the salt finger case, leading them to postulate that double diffusion may be responsible for some turbulent mixing events where Ri $> 1/4$.

REFERENCES

Batchelor, G. K., 1953: *The Theory of Homogeneous Turbulence.* Cambridge University Press, 197 pp.

Canuto, V. M., Y. Cheng, and A. M. Howard, 2008: A new model for double diffusion + turbulence. *Geophys. Res. Lett.,* **35,** L02613, doi:10.1029/2007GL032580.

Caplan, S., 2008: Microstructure signatures of equilibrium double-diffusive convection. MS thesis, Dept. of Oceanography, Naval Postgraduate School, 57 pp.

Carpenter, J. R., T. Sommer, and A. Wüest, 2012: Simulations of a double-diffusive interface in the diffusive convection regime. *J. Fluid Mech.,* **711,** 411–436, doi:10.1017/jfm.2012.399.

Davis, R. E., 1994: Diapycnal mixing in the ocean: The Osborn–Cox model. *J. Phys. Oceanogr.,* **24,** 2560–2576, doi:10.1175/1520-0485(1994)024<2560:DMITOT>2.0.CO;2.

Flanagan, J. D., A. S. Lefler, and T. Radko, 2013: Heat transport through diffusive interfaces. *Geophys. Res. Lett.,* **40,** 2466–2470, doi:10.1002/grl.50440.

Gregg, M. C., 1987: Diapycnal mixing in a thermocline: A review. *J. Geophys. Res.,* **92,** 5249–5286, doi:10.1029/JC092iC05p05249.

Howard, L. N., 1961: Note on a paper of John W. Miles. *J. Fluid Mech.,* **10,** 509–512, doi:10.1017/S0022112061000317.

Itsweire, E. C., J. R. Koseff, D. A. Briggs, and J. H. Ferziger, 1993: Turbulence in stratified shear flows: Implications for interpreting shear-induced mixing in the ocean. *J. Phys. Oceanogr.,* **23,** 1508–1522, doi:10.1175/1520-0485(1993)023<1508:TISSFI>2.0.CO;2.

Kelley, D. E., 1984: Effective diffusivities within oceanic staircases. *J. Geophys. Res.,* **89,** 10 484–10 488, doi:10.1029/JC089iC06p10484.

——, 1990: Fluxes through diffusive staircases: A new formulation. *J. Geophys. Res.,* **95,** 3365–3371, doi:10.1029/JC095iC03p03365.

Kimura, S., W. Smyth, and E. Kunze, 2011: Turbulence in a sheared, salt-fingering-favorable environment: Anisotropy and effective diffusivities. *J. Phys. Oceanogr.,* **41,** 1144–1159, doi:10.1175/2011JPO4543.1.

Kunze, E., 1994: A proposed flux constraint for salt fingers in shear. *J. Mar. Res.,* **52,** 999–1016, doi:10.1357/0022240943076867.

Marmorino, G. O., and D. R. Caldwell, 1976: Heat and salt transport through a diffusive thermohaline interface. *Deep-Sea Res. Oceanogr. Abstr.,* **23,** 59–67, doi:10.1016/0011-7471(76)90808-1.

Martinson, D. G., 1990: Evolution of the Southern Ocean winter mixed layer and sea ice: Open ocean deepwater formation and ventilation. *J. Geophys. Res.,* **95,** 11 641–11 654, doi:10.1029/JC095iC07p11641.

Miles, J. W., 1961: On the stability of heterogeneous flows. *J. Fluid Mech.,* **10,** 496–508, doi:10.1017/S0022112061000305.

Newell, T. A., 1984: Characteristics of a double-diffusive interface at high density stability ratios. *J. Fluid Mech.,* **149,** 385–401, doi:10.1017/S0022112084002718.

Oakey, N. S., 1988: Estimates of mixing inferred from temperature and velocity microstructure. *Small-Scale Turbulence and Mixing in the Ocean,* J. Nihoul and B. Namart, Eds., Elsevier, 239–248.

Osborn, T. R., 1980: Estimates of the local rate of vertical diffusion from dissipation measurements. *J. Phys. Oceanogr.,* **10,** 83–89, doi:10.1175/1520-0485(1980)010<0083:EOTLRO>2.0.CO;2.

——, and C. S. Cox, 1972: Oceanic fine structure. *Geophys. Fluid Dyn.,* **3,** 321–345, doi:10.1080/03091927208236085.

Padman, L., 1994: Momentum fluxes through sheared oceanic thermohaline steps. *J. Geophys. Res.,* **99,** 22 491–22 499, doi:10.1029/94JC01741.

——, and I. S. F. Jones, 1985: Richardson number statistics in the seasonal thermocline. *J. Phys. Oceanogr.,* **15,** 844–854, doi:10.1175/1520-0485(1985)015<0844:RNSITS>2.0.CO;2.

Radko, T., 2003: A mechanism for layer formation in a double-diffusive fluid. *J. Fluid Mech.,* **497,** 365–380, doi:10.1017/S0022112003006785.

——, 2008: The double-diffusive modon. *J. Fluid Mech.,* **609,** 59–85, doi:10.1017/S0022112008002127.

——, 2013: *Double-Diffusive Convection*. Cambridge University Press, 368 pp.

——, and M. E. Stern, 2011: Finescale instabilities of the double-diffusive shear flow. *J. Phys. Oceanogr.,* **41,** 571–585, doi:10.1175/2010JPO4459.1.

——, and D. P. Smith, 2012: Equilibrium transport in double-diffusive convection. *J. Fluid Mech.,* **692,** 5–27, doi:10.1017/jfm.2011.343.

Richardson, L. F., 1920: The supply of energy from and to atmospheric eddies. *Proc. Roy. Soc. London,* **97A,** 354–373, doi:10.1098/rspa.1920.0039.

Shaw, W., and T. Stanton, 2014: Dynamic and double-diffusive instabilities in a weak pycnocline. Part I: Observations of heat

flux and diffusivity in the vicinity of Maud Rise, Weddell Sea. *J. Phys. Oceanogr.,* **44,** 1973–1991, doi:10.1175/JPO-D-13-042.1.

Stellmach, S., A. Traxler, P. Garaud, N. Brummell, and T. Radko, 2011: Dynamics of fingering convection. Part 2: The formation of thermohaline staircases. *J. Fluid Mech.,* **677,** 554–571, doi:10.1017/jfm.2011.99.

Stern, M. E., T. Radko, and J. Simeonov, 2001: Salt fingers in an unbounded thermocline. *J. Mar. Res.,* **59,** 355–390, doi:10.1357/002224001762842244.

St. Laurent, L., and R. W. Schmitt, 1999: The contribution of salt fingers to vertical mixing in the North Atlantic tracer release experiment. *J. Phys. Oceanogr.,* **29,** 1404–1424, doi:10.1175/1520-0485(1999)029<1404:TCOSFT>2.0.CO;2.

Taylor, J., 1988: The fluxes across a diffusive interface at low values of the density ratio. *Deep-Sea Res.,* **35,** 555–567, doi:10.1016/0198-0149(88)90131-8.

Turner, J. S., 1965: The coupled turbulent transports of salt and heat across a sharp density interface. *Int. J. Heat Mass Transfer,* **8,** 759–767, doi:10.1016/0017-9310(65)90022-0.

Wells, M. G., and R. W. Griffiths, 2003: Interaction of salt finger convection with intermittent turbulence. *J. Geophys. Res.,* **108,** 3080, doi:10.1029/2002JC001427.

You, Y., 2002: A global ocean climatological atlas of the Turner angle: Implications for double-diffusion and water-mass structure. *Deep-Sea Res.,* **49,** 2075–2093, doi:10.1016/S0967-0637(02)00099-7.